Modeling of Complex Planetary Gear Sets Using Power-Oriented Graphs

Roberto Zanasi, *Member, IEEE*, and Davide Tebaldi

***Abstract*—In this paper, a systematic approach for the dynamic modeling of complex planetary gear sets is presented. The approach relies upon a set of rules for building the system matrices and vectors of the system full dynamic model for any planetary gear set. A congruent state-space transformation is applied to obtain a reduced-order rigid model of the system, which allows for faster simulations. The behavior of the tangential forces accounting for the gears interactions is proven to be obtained from the reduced-order model. Furthermore, the kinematic relations of the considered planetary gear set are automatically generated when developing the reduced-order rigid model. As an example, two systems of interest in the vehicle industry are then modeled with the proposed approach and simulated in Matlab/Simulink: a Ravigneaux planetary gear set and a double-stage planetary gear set.**

***Index Terms*—Automotive systems, planetary gear sets, energetic modeling, power-oriented graphs, simulation.**

I. Introduction

THE trend in the development of modern road transportation systems is strongly oriented toward the hybridization of propulsion systems, since this represents the most promising solution allowing to limit the exhaust emissions. The advantages that Hybrid Electric Vehicles (HEVs) can potentially bring to the world community are several. A vast array of different architectures have been proposed in the literature for the development of different HEVs topologies with different control strategies [1]–[2]. Based on the architecture type, it is possible to distinguish among series [3], parallel [4] and power-split [5]–[6] hybrid types. Among the variety of architectures, power-split HEVs definitely stick out, since they combine the advantages of series and parallel hybrid architectures [5]. Power-split HEVs exploit a device whose purpose is to split the power coming from the endothermic source of energy, i.e. the ICE (Internal Combustion Engine), into two different power flows driving the vehicle transmission system. The first power path is fully mechanical, whereas the second includes some mechanical-to-electrical and electrical-to-mechanical energy conversion. The mechanical power-splitting device is typically a planetary gear set, which can be of several types: single-stage [7], double-stage [8] or more articulated solutions for specific applications such as Ravigneaux planetary gear sets [9]–[11] and many others.

In order to achieve the full potential of HEVs, the power management problem must be solved. This is the problem of delivering the power demand from the transmission system while minimizing the specific fuel consumption of the ICE. The latter requirement can be achieved by performing a careful analysis of the most frequent operating points of all the physical elements of the architecture, with the final goal to make them work in the most efficient operating regions. The first step is therefore the mathematical modeling of the physical elements composing the architecture. This task is essential when developing the control strategy for the considered hybrid architecture, since it allows to carefully investigate its dynamic behavior and to properly control it. Different works can be found in the literature regarding the modeling of power-split HEVs, including planetary gear sets and all the main elements of the transmission system. When focusing on planetary gear sets, an interesting approach for easily and quickly determining the kinematics of a coupled epicyclic spur-gear train can be found in [12]. Next, the well-known Lever Analogy was introduced back in 1981 by Benford and Leising [13]. This is still nowadays one of the most effective tools for analyzing the kinematics and the dynamics of planetary gear sets. In fact, several works refer to the Lever Analogy to establish a fundamental understanding of the speed and torque relationships characterizing the considered planetary gear sets [5], [14]–[16]. In [17], the planetary gear set is modeled by using basic physics laws and introducing some simplifying assumptions about the mechanical dynamics, i.e. all the connections in the powertrain are supposed to be rigid. With all these methods, the natural constraints relating the gears angular speeds, as well as the input torques relations at steady-state, can be found. The mathematical modeling of physical systems can also be effectively derived by exploiting suitable modeling techniques [18]. Among those, the Power-Oriented Graphs (POG) technique [19] is adopted in this paper. The POG is a graphical modeling technique which relies on power and energy variables to describe the energy exchanges between the physical elements present in the system. Some examples showing the application of the POG technique in the automotive field can be found in [20]–[22].

In this paper, it is our intent to present an extension of the systematic approach for modeling planetary gear sets introduced in [22]. The contributions of this paper compared to our previous work are: a) formal proofs of the model properties; b) the introduction of the relative friction coefficients present between two

Manuscript received May 2, 2020; revised August 17, 2020 and October 20, 2020; accepted November 18, 2020. Date of publication November 27, 2020; date of current version January 22, 2021. The review of this article was coordinated by Dr. M. S. Ahmed. *(Corresponding author: Davide Tebaldi.)*

The authors are with the Department of Engineering "Enzo Ferrari" University of Modena and Reggio Emilia, Modena, MO 41125, Italy (e-mail: roberto.zanasi@unimore.it; davide.tebaldi@unimore.it).

Digital Object Identifier 10.1109/TVT.2020.3040899

in-contact gears; c) the comparison of the proposed method with the well-known Lever Analogy; d) new considerations about the possible operating conditions of planetary gear sets; e) the presentation of a new case study and its simulation in a power-split HEV; f) the extension of a case study, which was previously shown in our previous work [22], with the introduction of the relative friction coefficients; g) new considerations about the energy and the angular momentum of the system. The presented approach is deemed more effective than the current state of the art for the following reasons:

1) The dynamic model is *general* for any planetary gear set and is directly implementable in Matlab/Simulink.
2) The user is only required to compute two matrices, which fully and uniquely define the considered planetary gear set, using the algorithms presented in Section III. The procedure for building the system vectors and matrices is *entirely systematic*.
3) The model includes both the friction accounting for the rotation of the gears around their own axes and the *relative friction* associated with the in-contact gears exhibiting a relative movement.
4) Two state space models are obtained: a full dynamic model accounting for the gears elastic interaction, and a reduced-order model assuming rigid connections between the gears. The latter is proven suitable for fixed-step simulations.
5) In the reduced-order dynamic model, the time behavior of the tangential forces exchanged between the gears can still be obtained offline, even if the tangential forces are no longer present in the reduced-order model.
6) In the reduced-order dynamic model, the inherent kinematic speed and torque relations of the considered system automatically turn out.

The remainder of this paper is organized as follows. Section II concerns the introduction of the basic rules for the system definition. Next, the general full dynamic model and the POG scheme are introduced and described. In Section III, the direct computation of the radii matrix $\mathbf{R}$ and of the relative friction matrix $\mathbf{B}_{\Delta\omega}$ uniquely defining the system are addressed, followed by the derivation of the reduced-order model. In order to show how to use the proposed approach, we address the systematic modeling of two case studies: the Ravigneaux planetary gear set used in [9]–[11], see Section III, and a double-stage planetary gear set, see Section IV. In Section III, the comparison of the systematic POG-based approach with the Lever Analogy is addressed as well. Furthermore, the Ravigneaux planetary gear set model is tested with reference to a real case scenario. Finally, the conclusions of this work are given in Section V.

II. Modeling a Three-Gears System

This section focuses on the modeling of the three-gears system shown in Fig. 1. This system is used as a simple case study to introduce the notations adopted for the systematic modeling procedure presented in this paper. The horizontal colored arrows " → " " → " and " → " , shown in Fig. 1.a), highlight the orientation of the rotation axes of the three considered gears.

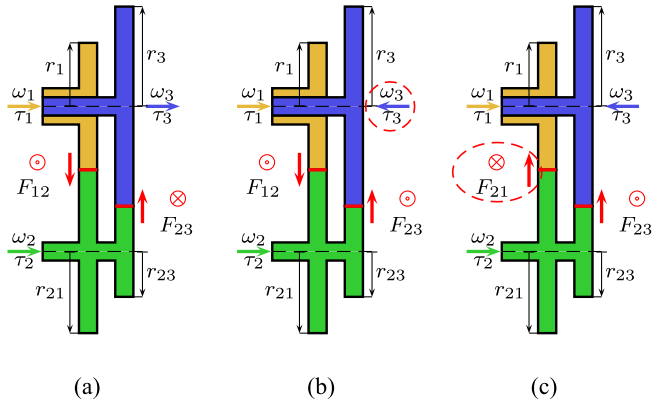

Fig. 1. Structure of the considered three-gears system.

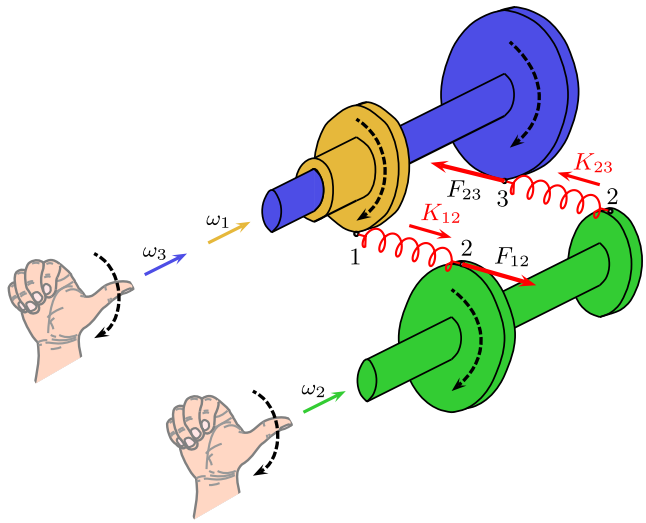

Fig. 2. Use of the Right-hand rule to compute: the positive direction of rotation of ω_1, ω_2 and ω_3; the positive orientation of F_{12} and F_{23}.

The same color coding is used in Fig. 2, showing the equivalent 3D representation of Fig. 1.a). By relying upon the well-known Right-hand rule and aligning the right thumb with the three colored arrows " → " " → " and → ", the reader can verify that the positive direction of rotation is clockwise for all the three angular speeds ω_1, ω_2 and ω_3. This is also highlighted by the black dashed arrows in Fig. 2. Additionally, the input torques τ_1, τ_2 and τ_3 are assumed to have the same *positive directions* as the respective angular speeds ω_1, ω_2 and ω_3, as denoted in Fig. 1. This ensures that the power flowing through the corresponding energetic port $(\omega_i,\ \tau_i)$ is positive if it is entering the system. Each gear is characterized by a one-digit subscript "i" and a specific color. The one-digit subscript "i" denotes all the parameters associated with the gear: J_i and b_i are the moment of inertia and the linear friction coefficient of gear "i". If two gears "i" and "j" are arranged in a mechanical configuration causing the presence of some relative friction between them, the symbol b_{ij} will denote the relative friction coefficient between gear "i" and gear "j".

The gears of the considered system interact with each other by means of their teeth, which represent an elastic coupling.

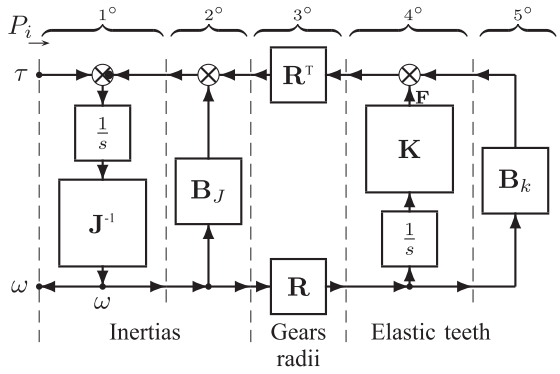

Fig. 3. General POG scheme of gearing systems.

This elastic coupling is denoted in Fig. 1 by red lines (i.e. "▬") representing the tangential springs acting between the gears. Each tangential spring is characterized by a subscript "ij". The term K_{ij} denotes the stiffness coefficient, whereas the variable F_{ij} denotes the tangential force associated with the spring "ij". The presence of these springs is also highlighted in the 3D drawing in Fig. 2, where the two tangential springs K_{12} and K_{23} are physically located at the contact points between the gears "1" and "2" and at the contact points between the gears "2" and "3", respectively.

The red vertical arrows "↓" "↑" shown in Fig. 1.a) highlight the *positive orientation* of both the tangential force F_{ij} and the tangential spring K_{ij}, for $ij \in \{12,\ 23\}$. As far as the system in Fig. 1.a) and Fig. 2 is concerned, it is possible to see that spring K_{12} has its first terminal connected to gear "1" and its second terminal connected to gear "2". Similarly, spring K_{23} has its first terminal connected to gear "2" and its second terminal connected to gear "3". Fig. 2 shows that the forces F_{12} and F_{23} exchanged at the contact points are indeed *tangential* to the gears, which is the reason why the contact springs are referred to as *tangential* springs. With reference to Fig. 2, the *positive direction* of forces F_{ij} can be determined as follows. Since the second terminal of spring K_{ij} is connected to gear J_j, the right thumb has to be aligned with the colored arrow identifying the positive direction of the angular speed ω_j. By applying the Right-hand rule, one finally obtains the *positive direction* of the tangential force F_{ij} associated with spring K_{ij}. With reference to Fig. 1, the positive direction of tangential force F_{ij} is:

1) entering the page (i.e. "⊗") if force F_{ij} is on the right-hand side of the horizontal arrow identifying the positive direction of angular speed ω_j;
2) exiting the page (i.e. "⊙") in the opposite case.

The subscript "ij" also denotes the linear friction coefficient d_{ij} in parallel with the tangential spring "ij".

The systematic modeling approach proposed in this paper allows to model any type of complex gear train, planetary or parallel gear set using the general POG scheme shown in Fig. 3. POG schemes are based on two fundamental blocks, namely the elaboration and the connection blocks [19]. The first is used to model all the physical elements storing and/or dissipating energy, while the second models all the physical elements performing energy conversion. Moving from left to right in the POG scheme of Fig. 3, the first block is an elaboration block describing the dynamics of the gears inertial elements present within the system. The second block is an elaboration block accounting for the gears viscous and relative friction. The third block is a connection block describing the energy conversion between the mechanical rotational and the mechanical translational energetic domains. The fourth block is an elaboration block accounting for the dynamics of the gears elastic contact points. Finally, the fifth block is an elaboration block describing the friction coefficients associated with the tangential springs. The crossed circles in the upper part of the elaboration blocks are called summation nodes. The presence of a black spot in a summation node means that the considered power variable entering the node has to be subtracted. By reading the POG scheme of Fig. 3, the following state space equations of the system can be directly obtained:

$$\underbrace{\begin{bmatrix}\mathbf{J} & \mathbf{0}\\ \mathbf{0} & \mathbf{K}^{-1}\end{bmatrix}}_{\mathbf{L}}\dot{\mathbf{x}} = \underbrace{\begin{bmatrix}-\mathbf{B}_J - \mathbf{R}^{\mathrm{T}}\mathbf{B}_k\mathbf{R} & -\mathbf{R}^{\mathrm{T}}\\ \mathbf{R} & \mathbf{0}\end{bmatrix}}_{\mathbf{A}}\mathbf{x} + \underbrace{\begin{bmatrix}\mathbf{I}\\ \mathbf{0}\end{bmatrix}}_{\mathbf{B}}\underbrace{\mathbf{u}}_{\boldsymbol{\tau}}, \tag{1}$$

where $\mathbf{x}$ is the state vector:

$$\mathbf{x} = \begin{bmatrix}\boldsymbol{\omega}\\ \mathbf{F}\end{bmatrix}, \qquad \boldsymbol{\omega} = \begin{bmatrix}\omega_1\\ \omega_2\\ \omega_3\end{bmatrix}, \qquad \mathbf{F} = \begin{bmatrix}F_{12}\\ F_{23}\end{bmatrix}, \tag{2}$$

$\boldsymbol{\omega}$ is the speed vector, $\mathbf{F}$ is the force vector, $\mathbf{u} = \boldsymbol{\tau}$ is the input torque vector and $\mathbf{y} = \mathbf{B}^{\mathrm{T}}\,\mathbf{x} = \boldsymbol{\omega}$ is the output vector. The meaning of the matrices within the state space model (1) is the following: $\mathbf{L}$, $\mathbf{A}$ and $\mathbf{B}$ are the energy, power and input-power matrices of the system, respectively; $\mathbf{I}$ is an identity matrix of proper dimension; $\mathbf{J}$ and $\mathbf{B}_J$ are the inertia and friction matrices related to the gears; $\mathbf{K}$ and $\mathbf{B}_K$ are the stiffness and friction matrices related to the tangential springs; $\mathbf{R}$ is the radii matrix defining the kinematic relations between the gears and the tangential springs. The friction matrix $\mathbf{B}_J$ is given by the sum of two terms:

$$\mathbf{B}_J = \mathbf{B}_\omega + \mathbf{B}_{\Delta\omega}. \tag{3}$$

The matrix $\mathbf{B}_\omega$ is the friction matrix associated with the rotation of the gears around their own rotation axes. The matrix $\mathbf{B}_{\Delta\omega}$ is the relative friction matrix associated with the relative angular speed between two different gears. The structures of matrices $\mathbf{J}$, $\mathbf{B}_\omega$, $\mathbf{K}$, $\mathbf{B}_K$ and vector $\boldsymbol{\tau}$ are:

$$\mathbf{J} = \begin{bmatrix}J_1 & 0 & 0\\ 0 & J_2 & 0\\ 0 & 0 & J_3\end{bmatrix}, \quad \mathbf{B}_\omega = \begin{bmatrix}b_1 & 0 & 0\\ 0 & b_2 & 0\\ 0 & 0 & b_3\end{bmatrix}, \quad \boldsymbol{\tau} = \begin{bmatrix}\tau_1\\ \tau_2\\ \tau_3\end{bmatrix}, \tag{4}$$

$$\mathbf{K} = \begin{bmatrix}K_{12} & 0\\ 0 & K_{23}\end{bmatrix}, \quad \mathbf{B}_K = \begin{bmatrix}d_{12} & 0\\ 0 & d_{23}\end{bmatrix}. \tag{5}$$

One can easily verify that: a) the structures of matrices $\mathbf{J}$, $\mathbf{B}_\omega$ and vector $\boldsymbol{\tau}$ in (4) are completely defined by the order of the angular speeds ω_i within the speed vector $\boldsymbol{\omega}$ defined in (2); b) the structures of matrices $\mathbf{K}$ and $\mathbf{B}_K$ in (5) are completely defined by the order of the tangential forces F_{ij} within the force vector $\mathbf{F}$ in (2). As the positive direction of the speeds ω_i and the positive orientation of the tangential forces F_{ij} change, only the radii matrix $\mathbf{R}$ and the relative friction matrix $\mathbf{B}_{\Delta\omega}$ vary. By adopting

the particular choice of positive directions and orientations as in Fig. 1.a), matrices $\mathbf{R}$ and $\mathbf{B}_{\Delta\omega}$ assume the following form:

$$\begin{matrix}12\\23\end{matrix}\ \mathbf{R}=\begin{matrix}\begin{bmatrix}1 & 2 & 3\\ -r_1 & -r_{21} & 0\\ 0 & r_{23} & r_3\end{bmatrix}\end{matrix},\qquad \begin{matrix}1\\2\\3\end{matrix}\ \mathbf{B}_{\Delta\omega}=\begin{matrix}\begin{bmatrix}1 & 2 & 3\\ b_{13} & 0 & -b_{13}\\ 0 & 0 & 0\\ -b_{13} & 0 & b_{13}\end{bmatrix}\end{matrix}, \tag{6}$$

The green terms in (6) denote the subscripts of the state space variables ω_i and F_{ij}. With reference to [19], one can prove that the following two statements hold:

1) The change of sign for the positive direction of the angular speed ω_i (and of torque τ_i) implies the change of sign for all the coefficients of: a) the i-th column of the radii matrix $\mathbf{R}$; b) the i-th column and the i-th row of the relative friction matrix $\mathbf{B}_{\Delta\omega}$.

Example. The gearing system in Fig. 1.b) differs from the one in Fig. 1.a) because the positive direction of the angular speed ω_3 has been changed. Using the Right-hand rule, as described in Fig. 2, one can conclude that the positive direction of rotation of the gear J_3 has now changed into counter-clockwise. The new structures of matrices $\mathbf{R}$ and $\mathbf{B}_{\Delta\omega}$ are the following:

$$\begin{matrix}12\\23\end{matrix}\ \mathbf{R}=\begin{matrix}\begin{bmatrix}1 & 2 & 3\\ -r_1 & -r_{21} & 0\\ 0 & r_{23} & -r_3\end{bmatrix}\end{matrix},\qquad \begin{matrix}1\\2\\3\end{matrix}\ \mathbf{B}_{\Delta\omega}=\begin{matrix}\begin{bmatrix}1 & 2 & 3\\ b_{13} & 0 & b_{13}\\ 0 & 0 & 0\\ b_{13} & 0 & b_{13}\end{bmatrix}\end{matrix}, \tag{7}$$

where the black coefficients have not changed sign with respect to (6). The red coefficients in (7) have changed their sign, whereas the blue coefficients in (7) are those whose sign has not changed because a double sign change has occurred.

According to statement 1), matrices $\mathbf{R}$ and $\mathbf{B}_{\Delta\omega}$ need to be updated as described next. Since the positive direction of ω_3 has changed, the signs of all the coefficients in the third column of matrix $\mathbf{R}$ in (6) need to be changed, as shown in (7). Additionally, the signs of all the coefficients in the third column and in the third row of $\mathbf{B}_{\Delta\omega}$ in (6) need to be changed, as shown in (7). The blue coefficient b_{13} belongs to both the third row and the third column of matrix $\mathbf{B}_{\Delta\omega}$. Consequently, the coefficient b_{13} changes sign twice.

2) The change of the positive orientation of the tangential forces F_{ij} implies the change of sign for all the coefficients of the ij-th row of the radii matrix $\mathbf{R}$.

Example. The gearing system in Fig. 1.c) differs from the system in Fig. 1.b) because the positive orientation of the tangential force F_{12} has been changed. As a consequence, the new structure of matrix $\mathbf{R}$ is the following:

$$\begin{matrix}12\\23\end{matrix}\ \mathbf{R}=\begin{matrix}\begin{bmatrix}1 & 2 & 3\\ r_1 & r_{21} & 0\\ 0 & r_{23} & -r_3\end{bmatrix}\end{matrix}. \tag{8}$$

The color coding is the same as in (7). According to statement 2), matrix $\mathbf{R}$ needs to be updated as follows. Since the positive orientation of F_{12} has changed, the signs of all the coefficients in the row corresponding to $i=1$ and $j=2$ of matrix $\mathbf{R}$ in (7), namely the first row, need to be changed, as shown in (8).

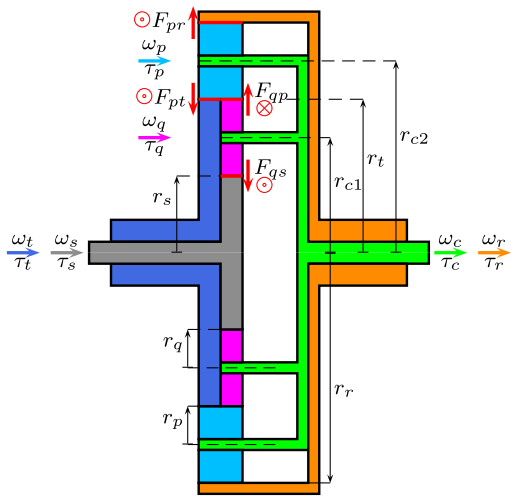

Fig. 4. Structure of the considered Ravigneaux planetary gear set.

III. Modeling a Ravigneaux Planetary Gear Set

Let us now consider the Ravigneaux planetary gear set shown in Fig. 4. This system has been studied and modeled in [9] using a different approach. Let us introduce the following symbols:

$$\begin{cases}\mathcal{N}_J=\{c,\ p,\ q,\ t,\ s,\ r\},\ n_J=\dim(\mathcal{N}_J)=6,\\ \mathcal{N}_K=\{pr,\ pt,\ qp,\ qs\},\ n_K=\dim(\mathcal{N}_K)=4,\\ \mathcal{N}_B=\{cp,\ cq,\ cr,\ st\},\ \ n_B=\dim(\mathcal{N}_B)=4,\end{cases} \tag{9}$$

where $\mathcal{N}_J$ is the set containing the one-digit subscripts identifying the system gears, n_J is the number of gears, $\mathcal{N}_K$ is the set containing the two-digit subscripts identifying the tangential springs, n_K is the number of tangential springs, $\mathcal{N}_B$ is the set containing all the two-digit subscripts identifying the relative friction coefficients b_{ij} and n_B is the number of relative friction elements present within the system.

The considered system can be modeled using the general POG block scheme shown in Fig. 3. The corresponding state space equations are given in (1). Let us choose the speed vector $\boldsymbol{\omega}$ and the force vector $\mathbf{F}$ as:

$$\boldsymbol{\omega}=\begin{bmatrix}\omega_c\\ \omega_p\\ \omega_q\\ \omega_t\\ \omega_s\\ \omega_r\end{bmatrix},\qquad \mathbf{F}=\begin{bmatrix}F_{pr}\\ F_{pt}\\ F_{qp}\\ F_{qs}\end{bmatrix}. \tag{10}$$

The order of the speed variables ω_i in $\boldsymbol{\omega}$ completely defines the structures of matrices $\mathbf{J}$, $\mathbf{B}_\omega$ and vector $\boldsymbol{\tau}$:

$$\mathbf{J}=\begin{bmatrix}J_c & 0 & 0 & 0 & 0 & 0\\ 0 & J_p & 0 & 0 & 0 & 0\\ 0 & 0 & J_q & 0 & 0 & 0\\ 0 & 0 & 0 & J_t & 0 & 0\\ 0 & 0 & 0 & 0 & J_s & 0\\ 0 & 0 & 0 & 0 & 0 & J_r\end{bmatrix},\ \mathbf{B}_\omega=\begin{bmatrix}b_c & 0 & 0 & 0 & 0 & 0\\ 0 & b_p & 0 & 0 & 0 & 0\\ 0 & 0 & b_q & 0 & 0 & 0\\ 0 & 0 & 0 & b_t & 0 & 0\\ 0 & 0 & 0 & 0 & b_s & 0\\ 0 & 0 & 0 & 0 & 0 & b_r\end{bmatrix},\ \boldsymbol{\tau}=\begin{bmatrix}\tau_c\\ \tau_p\\ \tau_q\\ \tau_t\\ \tau_s\\ \tau_r\end{bmatrix}. \tag{11}$$

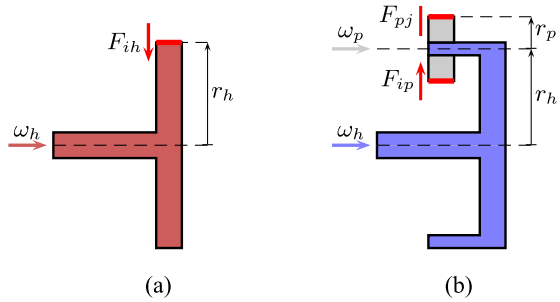

Fig. 5. Effective radii r_h. (a) Direct contact. (b) Indirect contact.

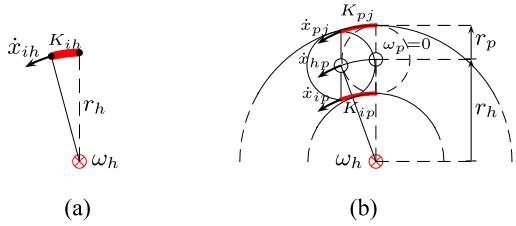

Fig. 6. Angular speeds ω_h and tangential velocities $\dot{x}_{hj}$. (a) Direct contact. (b) Indirect contact.

The order of the force variables F_{ij} within vector $\mathbf{F}$ in (10) completely defines the structures of matrices $\mathbf{K}$ and $\mathbf{B}_K$:

$$\mathbf{K}=\begin{bmatrix} K_{pr} & 0 & 0 & 0 \\ 0 & K_{pt} & 0 & 0 \\ 0 & 0 & K_{qp} & 0 \\ 0 & 0 & 0 & K_{qs} \end{bmatrix}, \quad \mathbf{B}_K=\begin{bmatrix} d_{pr} & 0 & 0 & 0 \\ 0 & d_{pt} & 0 & 0 \\ 0 & 0 & d_{qp} & 0 \\ 0 & 0 & 0 & d_{qs} \end{bmatrix}. \tag{12}$$

The only two matrices which are not yet defined in (1) are the radii matrix $\mathbf{R}$ and the relative friction matrix $\mathbf{B}_{\Delta\omega}$.

A. Algorithm 1: Calculation of Radii Matrix $\mathbf{R}$.

Let $r_{ij,h}$ denote the generic coefficient of matrix $\mathbf{R}=[r_{ij,h}]$, where $ij \in \mathcal{N}_K$ and $h \in \mathcal{N}_J$, see (9). Coefficient $r_{ij,h}$ links the angular speed ω_h of gear h to the tangential speed of one of the two terminals of the tangential force F_{ij}.

Property 1: The generic coefficient $r_{ij,h}$ of the radii matrix $\mathbf{R}$ can be computed as follows:

$$r_{ij,h} = S_{F_{ij}}\, S_{\omega_h}\, r_h, \tag{13}$$

where:

a) r_h is the "effective radius" *which links the angular speed ω_h to the tangential force F_{ij}. We distinguish the two cases: 1) if the angular speed ω_h directly affects the force F_{ij}, see the direct contact of Fig. 5(a), then the effective radius r_h coincides with the radius of the gear which links velocity ω_h to force F_{ij}; 2) if the angular speed ω_h affects the force F_{ij} through an intermediate gear "p", see the indirect contacts of Fig. 5.b, then the effective radius r_h coincides with the distance between the rotation axes of the two angular speeds ω_h and ω_p.*

b) $S_{F_{ij}}$ is the sign of the positive orientation of vector F_{ij}:

$$S_{F_{ij}} = \begin{cases} 1 & \text{if } i=h \text{ (direct) or } i=p \text{ (indirect)}, \\ -1 & \text{if } j=h \text{ (direct) or } j=p \text{ (indirect)}. \end{cases}$$

c) S_{ω_h} is related to the sign of the velocity vector ω_h:

$$S_{\omega_h} = \begin{cases} 1 & \text{if force } F_{ij} \text{ is on the left of vector } \omega_h, \\ -1 & \text{if force } F_{ij} \text{ is on the right of vector } \omega_h. \end{cases}$$

The left and right sides of vector ω_h are determined by moving along the positive direction of vector ω_h.

Example. By applying the previous rules to the gears shown in Fig. 5, one obtains: a) the coefficient $r_{ih,h}$ associated with the "direct" contact is $r_{ih,h}=-r_h$ because $S_{F_{ih}}=-1$ and $S_{\omega_h}=1$; b) the coefficients $r_{pj,h}$ and $r_{ip,h}$ associated with the "indirect" contacts are: $r_{pj,h}=r_h$ because $S_{F_{pj}}=1$ and $S_{\omega_h}=1$; $r_{ip,h}=-r_h$ because $S_{F_{ip}}=-1$ and $S_{\omega_h}=1$.

From (1), it can be easily shown that $\dot{x}_{ij}=r_{ij,h}\,\omega_h$ is the tangential speed of one of the two terminals of the spring K_{ij} when the angular speed ω_h moves along its positive direction. Since the sign of $\dot{x}_{ij}$ directly affects the sign of F_{ij}, it results that $\dot{x}_{ij}$ must change sign both when the velocity vector ω_h and the force vector F_{ij} change their positive direction. Fig. 6 graphically shows why the *effective radii* are equal to r_h for both the cases a) and b) of direct and indirect contact. In particular, with reference to the indirect contact case b), the tangential speed $\dot{x}_{hp}=r_h\,\omega_h$ is equal to the tangential speeds $\dot{x}_{pj}$ and $\dot{x}_{ip}$ of the two elastic elements K_{pj} and K_{ip}. This holds because the angular speed ω_p is kept equal to zero when ω_h moves along its positive direction.

By applying the systematic rules given in Prop. 1 to the Ravigneaux planetary gear set of Fig. 4, one obtains the following radii matrix $\mathbf{R}$:

$$\mathbf{R}=\begin{array}{c} \\ pr \\ pt \\ qp \\ qs \end{array}\!\!\begin{array}{c} \begin{array}{cccccc} c & p & q & t & s & r \end{array} \\ \begin{bmatrix} r_{c2} & r_p & 0 & 0 & 0 & -r_r \\ r_{c2} & -r_p & 0 & -r_t & 0 & 0 \\ r_{c1}-r_{c2} & r_p & r_q & 0 & 0 & 0 \\ r_{c1} & 0 & -r_q & 0 & -r_s & 0 \end{bmatrix} \end{array}. \tag{14}$$

The coefficient $r_{qp,c}=r_{c1}-r_{c2}$ highlighted in (14) describes the interaction between the angular speed ω_c and the tangential force F_{qp}. This coefficient is obtained using the superposition principle: a) the first term $r'_{qp,c}=r_{c1}$ is related to ω_c affecting F_{qp} through gear "q", being r_{c1} the effective radius, for which: $S_{F_{qp}}=1$ and $S_{\omega_c}=1$ hold; b) the second term $r''_{qp,c}=-r_{c2}$ is related to ω_c affecting F_{qp} through gear "p", being r_{c2} the effective radius, for which $S_{F_{qp}}=-1$ and $S_{\omega_c}=1$ hold. The parameters within the radii matrix $\mathbf{R}$ in (14) are constrained as follows:

$$\begin{aligned} r_q &= \frac{r_t}{2}-\frac{r_s}{2}, & r_p &= \frac{r_r}{2}-\frac{r_t}{2}, \\ r_{c1} &= \frac{r_s}{2}+\frac{r_t}{2}, & r_{c2} &= \frac{r_r}{2}+\frac{r_t}{2}. \end{aligned} \tag{15}$$

The constraints in (15) easily follow from Fig. 4. Substituting (15) in (14), one obtains the following equivalent form of the

radii matrix $\mathbf{R}$:

$$\begin{array}{c} \\ pr \\ pt \\ qp \\ qs \end{array} \begin{array}{c} \begin{array}{cccccc} c & p & q & t & s & r \end{array} \\ \mathbf{R}= \begin{bmatrix} \frac{r_r}{2}+\frac{r_t}{2} & \frac{r_r}{2}-\frac{r_t}{2} & 0 & 0 & 0 & -r_r \\ \frac{r_r}{2}+\frac{r_t}{2} & \frac{r_t}{2}-\frac{r_r}{2} & 0 & -r_t & 0 & 0 \\ \frac{r_s}{2}-\frac{r_r}{2} & \frac{r_r}{2}-\frac{r_t}{2} & \frac{r_t}{2}-\frac{r_s}{2} & 0 & 0 & 0 \\ \frac{r_s}{2}+\frac{r_t}{2} & 0 & \frac{r_s}{2}-\frac{r_t}{2} & 0 & -r_s & 0 \end{bmatrix} \end{array}. \quad (16)$$

Remark 1: Let us consider all the planetary gear sets that can rotate along a fixed axis when all the gears in the set are locked together. As an example, refer to the case studies shown in Fig. 4 and Fig. 16. Let $\mathbf{d}_\omega = [d_1\ d_2\ \ldots\ d_{n_J}]^{\mathrm{T}}$ denote a vector whose components d_i are defined as follows:

$$d_i = \begin{cases} 1 & \text{if the vectors } \vec{\omega}_i \text{ and } \vec{\omega}_1 \text{ have the same direction,} \\ -1 & \text{otherwise.} \end{cases}$$

One can easily verify that, for the considered planetary gear sets, vector $\mathbf{d}_\omega$ belongs to the kernel of matrix $\mathbf{R}$, that is $\mathbf{R}\,\mathbf{d}_\omega = 0$. As far as the Ravigneaux planetary gear set in Fig. 4 is concerned, $d_i = 1$ holds for $i = [1,\ 2,\ \ldots,\ n_J]$. Therefore, the relation $\mathbf{R}\,\mathbf{d}_\omega = 0$ implies that the sum of all the elements contained within each row of matrix $\mathbf{R}$ equals zero. This property can be easily proven true by referring to the matrix $\mathbf{R}$ in (16) as an example. From a physical point of view, this property means that $d_1\omega_1 = d_2\omega_2 = \ldots = d_{n_J}\omega_{n_J} \neq 0$ is a feasible operating condition for the considered system. Note: this property does not apply to the three-gears system in Fig. 1.

B. Algorithm 2: Calculation of Relative Friction Matrix $\mathbf{B}_{\Delta\omega}$.

Let B_{ij} denote the generic coefficient of matrix $\mathbf{B}_{\Delta\omega} = [B_{ij}]$ where $i, j \in \mathcal{N}_J$, with the set $\mathcal{N}_J$ is defined in (9).

Property 2: The generic coefficient B_{ij} of the relative friction matrix $\mathbf{B}_{\Delta\omega}$ can be computed as:

$$B_{ij} = \begin{cases} \displaystyle\sum_{pq \in \mathcal{N}_i} b_{pq} & \text{if} \quad i = j, \\ S_{ij}\bar{b}_{ij} & \text{if} \quad i \neq j, \end{cases} \quad (17)$$

where $\mathcal{N}_i$ is a set of subscripts "pq" defined as follows:

$$\mathcal{N}_i = \{\text{all the subscripts } pq \in \mathcal{N}_B \text{ such that } p = i \text{ or } q = i\}$$

$\mathcal{N}_B$ is defined in (9), $\bar{b}_{ij}$ is the relative friction coefficient defined as:

$$\bar{b}_{ij} = \begin{cases} b_{ij} & \text{if} \quad ij \in \mathcal{N}_B, \\ b_{ji} & \text{if} \quad ji \in \mathcal{N}_B, \\ 0 & \text{if} \quad \text{otherwise,} \end{cases}$$

and S_{ij} is a sign function defined as:

$$S_{ij} = \begin{cases} -1 & \text{if } \omega_i \text{ and } \omega_j \text{ have the same positive direction,} \\ 1 & \text{if } \omega_i \text{ and } \omega_j \text{ have different positive direction,} \\ 0 & \text{if } \bar{b}_{ij} = 0. \end{cases}$$

Note: according to (17), all the coefficients B_{ii} on the diagonal of matrix $\mathbf{B}_{\Delta\omega}$ are always positive.

Applying the systematic rules given in Prop. 2, one can build the following relative friction matrix $\mathbf{B}_{\Delta\omega}$ for the considered Ravigneaux planetary gear set:

$$\begin{array}{c} \\ c \\ p \\ q \\ t \\ s \\ r \end{array} \begin{array}{c} \begin{array}{cccccc} c & p & q & t & s & r \end{array} \\ \mathbf{B}_{\Delta\omega}= \begin{bmatrix} b_{cp}+b_{cq}+b_{cr} & -b_{cp} & -b_{cq} & 0 & 0 & -b_{cr} \\ -b_{cp} & b_{cp} & 0 & 0 & 0 & 0 \\ -b_{cq} & 0 & b_{cq} & 0 & 0 & 0 \\ 0 & 0 & 0 & b_{st} & -b_{st} & 0 \\ 0 & 0 & 0 & -b_{st} & b_{st} & 0 \\ -b_{cr} & 0 & 0 & 0 & 0 & b_{cr} \end{bmatrix} \end{array}. \quad (18)$$

The generic relative friction coefficient b_{ij} within matrix $\mathbf{B}_{\Delta\omega}$, acting in between gears "i" and "j", can have two different meanings. In fact, it can either be an actual relative friction coefficient within the system or be used to represent a lockup clutch between the two gears. The two limit cases of $b_{ij} \to 0$ and $b_{ij} \to b_{ij}^{\infty}$, where b_{ij}^{∞} has to be sufficiently large, represent the case of open and closed lockup clutch, respectively. This enables the simulation of different operating modes of the transmission system. The proposed model also allows to apply a nonlinear control to a lockup clutch inserted in between two gears of the system: this can be done by inserting an external control acting on the system input and output vectors $\mathbf{u} = \boldsymbol{\tau}$ and $\mathbf{y} = \boldsymbol{\omega}$.

The vectors and the matrices defined in (10), (11), (12), (14) and (18) completely define the full elastic model (1) of the considered Ravigneaux planetary gear set.

C. Ravigneaux Planetary Gear Set: Reduced-Order Rigid Model.

Let us assume all the coefficients K_{ij}, for $ij \in \mathcal{N}_K$, within the stiffness matrix $\mathbf{K}$ in (12) to tend to infinity. From the state space model (1), one obtains the following $n_K = 4$ constraints among the gears angular speeds:

$$\mathbf{R}\,\boldsymbol{\omega} = \mathbf{0} \ \Leftrightarrow \ \begin{cases} r_{c2}\,\omega_c + r_p\,\omega_p - r_r\,\omega_r = 0, \\ r_{c2}\,\omega_c - r_p\,\omega_p - r_t\,\omega_t = 0, \\ r_p\,\omega_p + r_q\,\omega_q + \omega_c(r_{c1} - r_{c2}) = 0, \\ r_{c1}\,\omega_c - r_q\,\omega_q - r_s\,\omega_s = 0. \end{cases} \quad (19)$$

These constraints can be used to express n_K angular speeds of the system as a function of the remaining $n_r = n_J - n_K = 2$ angular speeds. The integer n_r also represents the order of the reduced-order rigid model obtained when $\mathbf{K} \to \infty$. Let $\mathbf{x}_1 = [\ \omega_c\ \ \omega_r\ ]^{\mathrm{T}}$ be the state vector of the reduced-order rigid model. Using constraints (19) and (15), the original state vector $\mathbf{x}$ can be expressed as a function of the new state vector $\mathbf{x}_1$ as:

$$\mathbf{x} = \mathbf{T}_1\,\mathbf{x}_1 \quad \Leftrightarrow \quad \underbrace{\begin{bmatrix} \boldsymbol{\omega} \\ \mathbf{F} \end{bmatrix}}_{\mathbf{x}} = \underbrace{\begin{bmatrix} \mathbf{Q}_1 \\ \mathbf{0} \end{bmatrix}}_{\mathbf{T}_1} \underbrace{\begin{bmatrix} \omega_c \\ \omega_r \end{bmatrix}}_{\mathbf{x}_1},$$

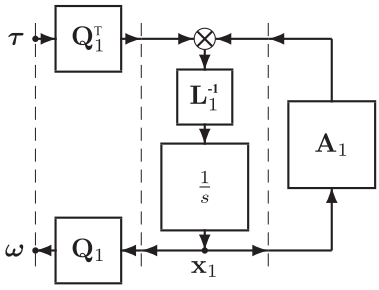

Fig. 7. Reduced-order rigid POG scheme of gearing systems.

where the matrix $\mathbf{Q}_1$ is defined as follows:

$$\boldsymbol{\omega} = \mathbf{Q}_1 \, \mathbf{x}_1 \quad \Leftrightarrow \quad \mathbf{Q}_1 = \begin{bmatrix} 1 & 0 \\ -\frac{n_1-1}{n_1+1} & \frac{2n_1}{n_1+1} \\ \frac{n_1+n_2-2n_1n_2}{n_1+n_2} & \frac{2n_1n_2}{n_1+n_2} \\ 1-n_1 & n_1 \\ 1-n_2 & n_2 \\ 0 & 1 \end{bmatrix}. \tag{20}$$

The parameters n_1 and n_2 in (20) denote the *ring-over-large sun* and the *ring-over-small sun* gear ratios, respectively:

$$n_1 = -r_r/r_t, \qquad n_2 = r_r/r_s. \tag{21}$$

By applying the congruent transformation $\mathbf{x} = \mathbf{T}_1 \, \mathbf{x}_1$ to system (1), see [19], one obtains the following state space model $\mathbf{L}_1 \dot{\mathbf{x}}_1 = \mathbf{A}_1 \mathbf{x}_1 + \mathbf{B}_1 \mathbf{u}$ of the reduced-order rigid system:

$$\underbrace{\begin{bmatrix} J_{11} & J_{12} \\ J_{12} & J_{22} \end{bmatrix}}_{\mathbf{L}_1} \dot{\mathbf{x}}_1 = \underbrace{\begin{bmatrix} a_{11} & a_{12} \\ a_{12} & a_{22} \end{bmatrix}}_{\mathbf{A}_1} \mathbf{x}_1 + \underbrace{\mathbf{Q}_1^{\mathrm{T}}}_{\mathbf{B}_1} \underbrace{\boldsymbol{\tau}}_{\mathbf{u}}, \tag{22}$$

where matrices $\mathbf{L}_1$, $\mathbf{A}_1$ and $\mathbf{B}_1$ have the following structure:

$$\begin{cases} \mathbf{L}_1 = \mathbf{T}_1^{\mathrm{T}} \mathbf{L} \, \mathbf{T}_1 = \mathbf{Q}_1^{\mathrm{T}} \mathbf{J} \, \mathbf{Q}_1, \\ \mathbf{A}_1 = \mathbf{T}_1^{\mathrm{T}} \mathbf{A} \, \mathbf{T}_1 = -\underbrace{\mathbf{Q}_1^{\mathrm{T}} \mathbf{R}^{\mathrm{T}} \mathbf{B}_K \mathbf{R} \, \mathbf{Q}_1}_{\mathbf{0}} - \mathbf{Q}_1^{\mathrm{T}} \mathbf{B}_J \mathbf{Q}_1, \\ \mathbf{B}_1 = \mathbf{T}_1^{\mathrm{T}} \mathbf{B} = \mathbf{Q}_1^{\mathrm{T}}. \end{cases} \tag{23}$$

The term $\mathbf{Q}_1^{\mathrm{T}} \mathbf{R}^{\mathrm{T}} \mathbf{B}_K \mathbf{R} \, \mathbf{Q}_1$ in (23) is equal to zero because $\mathbf{Q}_1 \in \ker(\mathbf{R})$:

$$\mathbf{R} \, \boldsymbol{\omega} = \mathbf{0} \quad \Leftrightarrow \quad \mathbf{R} \, \mathbf{Q}_1 \, \mathbf{x}_1 = \mathbf{0} \quad \Leftrightarrow \quad \mathbf{R} \, \mathbf{Q}_1 = \mathbf{0}. \tag{24}$$

The full expressions of the elements L_{ij} and a_{ij} within the energy matrix $\mathbf{L}_1$ and the power matrix $\mathbf{A}_1$ are not reported for the sake of brevity, as they can be straightforwardly computed using (23). The reduced-order rigid model given in (22) can be graphically represented using the POG block scheme in Fig. 7.

The constraints among the angular speeds of the Ravigneaux planetary gear set that were derived in [9] using the Willis equation (see Eqs. (3)-(4) in [9]) are the same as those obtained using the presented systematic approach: see the fourth and fifth rows of system (20). Additionally, the static input torques balance given in Eqs. (5)-(6) in [9] is equivalent to the following constraint:

$$\mathbf{B}_1 \, \boldsymbol{\tau} = \mathbf{Q}_1^{\mathrm{T}} \, \boldsymbol{\tau} = 0. \tag{25}$$

The latter equation can be obtained at steady-state from the first equation of system (1) when $\mathbf{B}_J = 0$, that is when the friction terms within the system are neglected.

D. Calculation of the Vector Force $\mathbf{F}$.

The reduced-order rigid system (22) no longer contains any information regarding the force vector $\mathbf{F}$. Nevertheless, vector $\mathbf{F}$ can be obtained from the reduced-order rigid system (22), as described by Prop. 3 illustrated in the following.

Property 3: The time behavior of the force vector $\mathbf{F}$ can be obtained from the state vector $\mathbf{x}_1$ and the input vector $\mathbf{u} = \boldsymbol{\tau}$ of the reduced rigid system (22) using the following relation:

$$\mathbf{F} = (\mathbf{R}\mathbf{J}^{-1}\mathbf{R}^{\mathrm{T}})^{-1}\mathbf{R}\mathbf{J}^{-1}(\boldsymbol{\tau} - \mathbf{B}_J\mathbf{Q}_1\mathbf{x}_1). \tag{26}$$

The proof of this property is reported in Appendix.

Remark 2: The relation (26) can be very useful because it provides the tangential forces F_{ij} between the gears as a function of the input vector $\boldsymbol{\tau}$ and of the state vector $\mathbf{x}_1$ in the reduced-order rigid model (22). Note that relation (26) can be implemented offline.

E. Ravigneaux Planetary Gear Set: Lever Analogy.

A different approach for computing the kinematic relations of a planetary gear set is the Lever Analogy [13]. The considered Ravigneaux planetary gear set can be seen as the combination of two planetary gear sets:

i) a single planetary gear set $PG1$, where the sun, the planet pinions, the ring and the carrier are represented by gears "t", "p", "r" and "c", respectively;
ii) a planetary gear set $PG2$ with two sets of planet pinions, where the sun, the outer planet pinions, the inner planet pinions, the ring and the carrier are represented by gears "s", "p", "q", "r" and "c", respectively.

$PG1$ and $PG2$ share the same ring and the same carrier inertial elements. The procedure to follow in order to build a Lever Diagram [13] is the following:

1) replacement of each gear with a vertical lever;
2) rescaling, interconnection and/or combination of levers accordingly;
3) identification of the lever connections, according to the gears connections.

The lever diagrams of the two planetary gear sets $PG1$ and $PG2$ are shown in Fig. 8.a). The interconnections between the gears are denoted in Fig. 8.a) by horizontal links [13] highlighted in magenta. The whole lever diagram of the Ravigneaux planetary gear set [23] is obtained by rescaling the diagram of $PG1$ with respect to the diagram of $PG2$ according to the following proportion:

$$r_r : r_x = r_t : r_s.$$

The resulting diagram is shown in Fig. 8.b). In order to derive the kinematic relations between the angular speeds ω_i, two different scenarios can be considered. In the first scenario, gear "c" is held fixed and gear "r" rotates clockwise. In the second scenario, gear "r" is held fixed and gear "c" rotates clockwise. By applying the superposition principle to these two scenarios, one obtains the

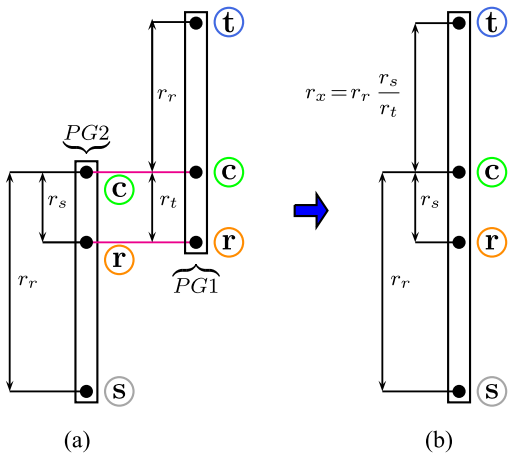

Fig. 8. Ravigneaux planetary gear set: Lever Diagrams.

following speed equations:

$$\omega_t = \omega_c\left(1+\frac{r_r}{r_t}\right)-\omega_r\frac{r_r}{r_t},\quad \omega_s = \omega_c\left(1-\frac{r_r}{r_s}\right)+\omega_r\frac{r_r}{r_s},$$

which coincide with those reported in the fourth and fifth rows of system (20) using (21). In order to derive the torque equations, two torque balances can be applied, considering the ring first and the carrier next as fulcrum, respectively. The obtained torque equations coincide with those given by constraint (25). The rotational inertias can finally be included in the diagram by attaching masses to the lever and solving force and moment balance equations [13].

F. Systematic POG-Based Approach Versus Lever Analogy

The main differences between the POG-based approach and the Lever Analogy approach are listed in the following:

a) *In the POG-based approach, step 1) of the Lever Diagram procedure reported in Section III-E is replaced by the drawing of a simple 2D graphical representation of the considered planetary gear set, such as the one shown in Fig. 4.*

b) *In the POG-based approach, step 2) of the Lever Diagram procedure is not required, since the elements in common to $PG1$ and $PG2$ are not treated as two separated elements, but as a unique inertial element interacting with $PG1$ and $PG2$.*

c) *In the POG-based approach, step 3) of the Lever Diagram procedure is automatically incorporated in the definition of set $\mathcal{N}_J$, set $\mathcal{N}_K$ and set $\mathcal{N}_B$.*

d) *The POG-based approach gives both a full dynamic model and a reduced-order rigid model of the considered system.*

The reduced-order model allows for faster simulations. Furthermore, the behavior of the forces that are exchanged at the gears contact points is not lost, as it can be recovered using Prop. 3.

The POG-based approach proposed in this paper offers the advantages of being systematic, flexible, and of providing a *general model which is directly implementable in the Matlab/Simulink environment*. The systematic property refers to the fact that the procedure for building the model lies on two simple algorithms which can be automatically implemented, once sets $\mathcal{N}_J$, $\mathcal{N}_K$ and $\mathcal{N}_B$ are defined. The flexibility property refers to the fact that the user can very easily choose which relative frictions b_{ij} must be present in the system by defining set $\mathcal{N}_B$. Additionally, the user can freely choose which angular speeds ω_i are to be kept in the state vector of the reduced-order rigid model. The general scheme shown in Fig. 3 can be used to model any planetary gear set, and is composed of basic blocks that can be found in the standard Simulink libraries.

In conclusion, the Lever Analogy is mainly suitable for the system kinematic analysis and gives a good understanding of the system thanks to the intuitive comparison with levers. On the other hand, the proposed systematic POG-based approach is suitable for simulation and control purposes. This is thanks to the fact that the system model is general and directly implementable in the Matlab/Simulink environment, and thanks to the fact that the system matrices and vectors are systematically built.

TABLE I
RAVIGNEAUX PLANETARY GEAR SET: SIMULATION PARAMETERS

$r_r = 21$ cm	$J_c = 17280$ kg mm^2
$r_s = 7$ cm	$J_p = 3456$ kg mm^2
$r_t = 10.5$ cm	$J_q = 1728$ kg mm^2
$r_q = 1.75$ cm	$J_t = 8640$ kg mm^2
$r_p = 5.25$ cm	$J_s = 5184$ kg mm^2
$r_{c1} = 8.75$ cm	$J_r = 15552$ kg mm^2
$r_{c2} = 15.75$ cm	$b_c = 0.01$ Nm/rpm
$b_p = b_q = b_t = b_c$	$b_s = b_r = b_c$
$b_{st} = 0.01$ Nm/rpm	$b_{cr} = b_{cq} = b_{cp} = b_{st}$
$K_{pt} = K_{pr} = 300000$ N/mm	$K_{qp} = K_{qs} = K_{pt}$
$d_{pt} = 0.1$ N sec/cm	$d_{pr} = d_{qp} = d_{qs} = d_{pt}$
$\boldsymbol{\tau} = [\ 100\ 0\ 0\ 0\ 0\ 0\ ]^{\mathrm{T}}$ Nm	$\boldsymbol{\omega}_0$=[0 0 0 0 0 0]$^{\mathrm{T}}$ rpm, $\mathbf{F}_0$=[0 0 0 0]$^{\mathrm{T}}$ N

G. Ravigneaux Planetary Gear Set: Simulation Results.

The Ravigneaux planetary gear set of Fig. 4 has been simulated in order to compare the dynamic behavior and the simulation time of the following two models: the full elastic model given in (1) and the reduced-order rigid model given in (22). The two simulations described in Section III-G1 and Section III-G2 have been performed using the parameters, input signals and initial conditions given in Table I. The simulation results reported in Section III-G3 refer to a real case scenario, where the Ravigneaux planetary set gear is exploited as a power-split device in a HEV architecture.

1) First Simulation: this simulation has been performed adopting the positive directions shown in Fig. 4 for the angular speeds ω_i and for the tangential forces F_{ij}. The obtained simulation results are shown in Fig. 9. In particular, the time behavior of the angular speeds ω_i, for $i \in \mathcal{N}_J$, is shown on the left subplot of Fig. 9, whereas the time behavior of the tangential forces F_{ij}, for $ij \in \mathcal{N}_K$, is shown on the right subplot. The continuous colored characteristics within the figure refer to the simulation results obtained using the elastic state-space model (1). The red dashed characteristics of angular speeds ω_i on the left subplot of Fig. 9 refer to the simulation results obtained using the rigid reduced-order model (22). The red dashed characteristics of the tangential forces F_{ij} on the right subplot of

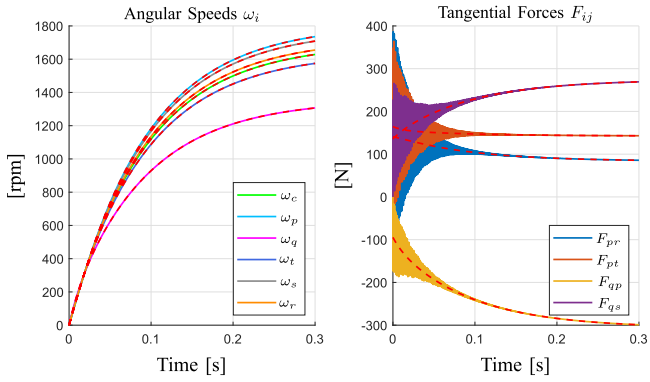

Fig. 9. First simulation of the Ravigneaux planetary gear set.

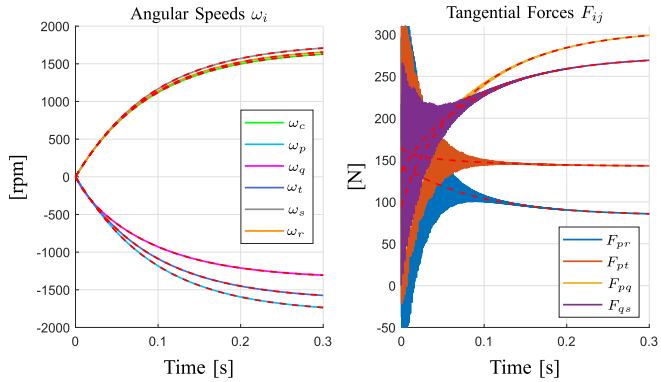

Fig. 10. Second simulation of the Ravigneaux planetary gear set.

Fig. 9 have been obtained offline using (26). Fig. 9 shows the good matching between the simulation results obtained using the full and reduced-order models. The right subplot of the figure shows the fast oscillations that the tangential forces F_{ij} exhibit. This is due to the fact that the stiffness coefficients K_{ij} in Table I are quite high, and the period of the forces oscillations is inversely proportional to the stiffness coefficients. It is possible to conclude that the full model is more suited to be used when accurate simulations need to be performed. In this way, the exact oscillating behavior of the tangential forces F_{ij} can be determined. Conversely, the reduced-order model is more suited to be used when real-time execution is sought. Fixed-step simulations are enabled by the reduced-order model, because the fast dynamics arising from the tangential springs are no longer present. Nevertheless, the average behavior of the tangential forces F_{ij} can still be recovered exploiting Prop. 3, as shown in the right subplot of Fig. 9.

2) Second Simulation: this simulation has been performed adopting the following positive directions for the variables ω_i and F_{ij} shown in Fig. 4:

$$\boldsymbol{\omega} = \begin{bmatrix} \omega_c \\ \omega_p \\ \omega_q \\ \omega_t \\ \omega_s \\ \omega_r \end{bmatrix}, \quad \mathbf{F} = \begin{bmatrix} F_{pr} \\ F_{pt} \\ F_{pq} \\ F_{qs} \end{bmatrix}. \tag{27}$$

The variables encircled in the red dashed ellipses in (27) are those whose sign has been changed with respect to positive directions reported in Fig. 4. Using the rules given in Prop. 1, one obtains the following new radii matrix $\mathbf{R}$:

$$\mathbf{R} = \begin{array}{c} \\ pr \\ pt \\ pq \\ qs \end{array} \begin{array}{c} \begin{array}{cccccc} c & p & q & t & s & r \end{array} \\ \begin{bmatrix} r_{c2} & -r_p & 0 & 0 & 0 & -r_r \\ r_{c2} & r_p & 0 & r_t & 0 & 0 \\ r_{c2} - r_{c1} & r_p & r_q & 0 & 0 & 0 \\ r_{c1} & 0 & r_q & 0 & -r_s & 0 \end{bmatrix} \end{array}. \tag{28}$$

The color coding for the coefficients in matrix $\mathbf{R}$ is the same as the one adopted in (7) for the three-gears system example. Indeed, the red coefficients and the red subscripts in (28) are those for which a sign change has occurred with respect to the radii matrix $\mathbf{R}$ shown in (14), according to statements 1) and 2) depicted in Section II. The new relative friction matrix $\mathbf{B}_{\Delta\omega}$ obtained using (27) and the rules given in Prop. 2 is the following:

$$\mathbf{B}_{\Delta\omega} = \begin{array}{c} \\ c \\ p \\ q \\ t \\ s \\ r \end{array} \begin{array}{c} \begin{array}{cccccc} c & p & q & t & s & r \end{array} \\ \begin{bmatrix} b_{cp}+b_{cq}+b_{cr} & b_{cp} & b_{cq} & 0 & 0 & -b_{cr} \\ b_{cp} & b_{cp} & 0 & 0 & 0 & 0 \\ b_{cq} & 0 & b_{cq} & 0 & 0 & 0 \\ 0 & 0 & 0 & b_{st} & b_{st} & 0 \\ 0 & 0 & 0 & b_{st} & b_{st} & 0 \\ -b_{cr} & 0 & 0 & 0 & 0 & b_{cr} \end{bmatrix} \end{array}. \tag{29}$$

The color coding for the coefficients in matrix $\mathbf{B}_{\Delta\omega}$ is the same as the one adopted in (7) for the three-gears system example. Indeed, the red coefficients and the red subscripts in (29) are those for which a sign change has occurred with respect to the friction matrix $\mathbf{B}_{\Delta\omega}$ given in (18), according to statement 1) depicted in Section II. The blue coefficients in (28) and in (29) are those whose sign has not changed because a double sign change has occurred. The simulation results obtained using (28) and (29) are shown in Fig. 10: the color and the meaning of the variables plotted in the figure are the same as in Fig. 9. Since the parameters, inputs and initial conditions are the same, the new simulation results coincide with those in Fig. 9 except for the sign of the power variables ω_p, ω_q, ω_t and F_{qp}. These changes of sign can be clearly noted by comparing the results reported in Fig. 9 and Fig. 10.

3) Third Simulation: reference is made to the power-split architecture of a hybrid agricultural vehicle shown in Fig. 11. The architecture is composed of three power sources. The first one is an ICE rigidly connected to gear "s". The other two power sources are the electric machines EM1 and EM2, which are rigidly connected to gears "t" and "r", respectively. The gear denoted by subscript "c" is rigidly connected to a 2-Speed gearbox, which allows for gear shifting in the considered architecture. The gearbox output shaft is connected to the load inertia J_L through a rotational spring K_L, which accounts for the gearbox elasticity. Furthermore, a friction coefficient d_L is associated with the rotational spring K_L, accounting for the losses occurring during the transients. The overall load inertia J_L includes the inertia of the gearbox output shaft, the inertia of the wheels through the differential, as well as the vehicle mass

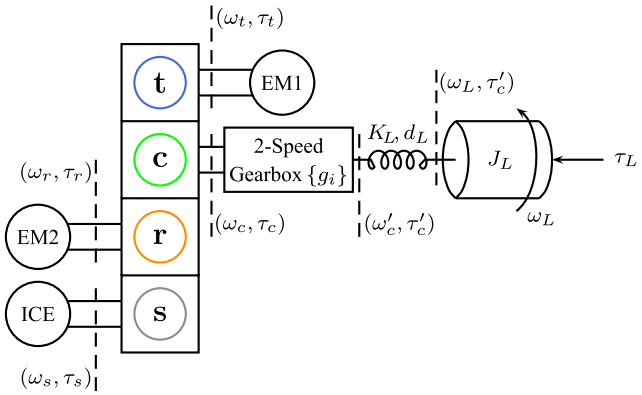

Fig. 11. Power-split architecture of a hybrid agricultural vehicle.

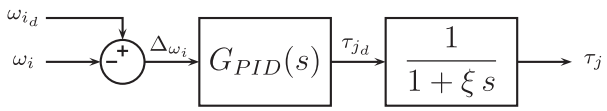

Fig. 12. Electric machines EM1 and EM2: control and modeling.

through the differential and the wheels radius. The external load torque τ_L accounts for the load that the transmission experiences when the agricultural vehicle is operating. Since the objective is to test the full and reduced-order dynamic models of the considered Ravigneaux planetary gear set, a simplified model has been adopted for the three power sources. The ICE is assumed to be a torque generator providing a constant torque $\tau_s = 820\,\text{Nm}$. Since the ICE is rigidly connected to gear "s", its inertia is included in J_s within matrix $\mathbf{J}$ in (11). In the considered scenario, the ICE is controlled to maintain a desired constant speed $\omega_{s_d} = 1400\,[\text{rpm}]$. The electric machines EM1 and EM2 are assumed to have a first-order step torque response with a time constant ξ. The considered first-order dynamics only accounts for the electric part of the machines, since EM1 and EM2 are rigidly connected to gears "t" and "r", respectively. A speed control is applied to each electric machine using two PID (Proportional-Integral-Derivative) regulators, as shown in Fig. 12. The two PID regulators are characterized by the following transfer function:

$$G_{PID}(s) = C_P\,(C_D\,s + 1) + \frac{C_P}{C_I\,s}, \tag{30}$$

where C_P, C_D and C_I are three design parameters. The PID regulator of EM2 determines a desired torque τ_{r_d} in order to keep the ICE speed ω_s equal to the desired speed target ω_{s_d}. Similarly, the PID regulator of EM1 determines a desired torque τ_{t_d} in order to make the gearbox input shaft speed ω_c follow the desired speed profile ω_{c_d}. The gearbox input and output shafts speeds ω_c and ω'_c are related as follows:

$$\omega'_c = \omega_c\; g_i,$$

where $g_i \in \{g_1,\ g_2\}$ is the engaged gear ratio. The angular speed ω'_c is equal to the load angular speed ω_L at steady-state, while they are slightly different during the transients because of the presence of the stiffness K_L. The positive directions of the angular speeds ω_i and of the tangential forces F_{ij} in the

TABLE II
ARCHITECTURE IN FIGS. 11 AND 12: TRANSMISSION PARAMETERS AND INITIAL CONDITIONS

$g_1 = 0.2296$	$g_2 = 0.7273$
$K_L = 50$ kNm/°	$d_L = 42$ Nm/rpm
$J_L = 19.16$ kg m^2	$C_P = 80.75$
$C_D = 0.12 \cdot 10^{-3}$	$C_I = 0.24$
$\xi = 4.7$ ms	$\boldsymbol{\omega}_0$=[0 0 0 0 1400 0]$^{\text{T}}$ rpm, $\mathbf{F}_0$=[0 0 0 0]$^{\text{T}}$ N

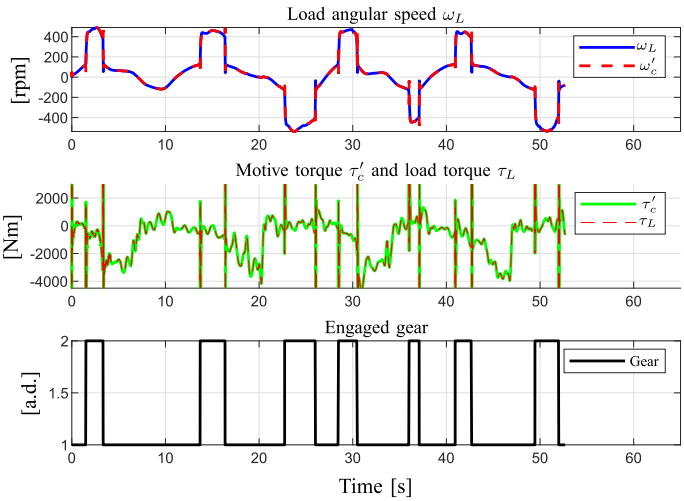

Fig. 13. Hybrid agricultural vehicle: simulation results from the gearbox to the load.

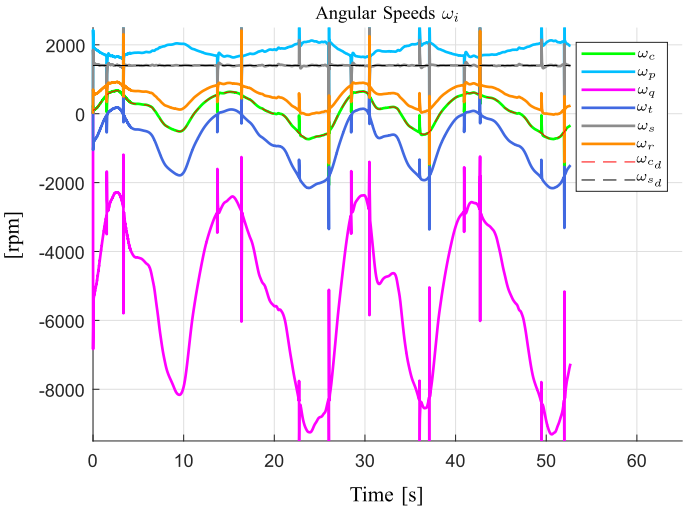

Fig. 14. Hybrid agricultural vehicle: angular speeds of the Ravigneaux planetary gear set.

Ravigneaux planetary gear set are those given in Fig. 4, whereas the planetary gear set parameters are those given in Table I. The parameters of the mechanical transmission connected to the carrier "c" and the initial conditions of the system are reported in Table II. The simulation results of the controlled system are shown in Fig. 13, Fig. 14 and. Fig. 15. The time behaviors of the load speed ω_L, the gearbox output shaft speed ω'_c, the motive torque τ'_c, the load torque τ_L and of the engaged gear signal are shown in Fig. 13. The profile of the load torque τ_L

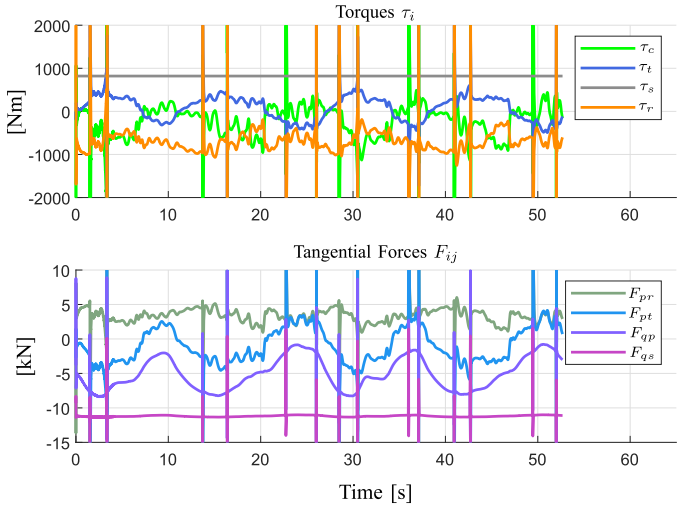

Fig. 15. Hybrid agricultural vehicle: torques and tangential contact forces of the Ravigneaux planetary gear set.

has been chosen to simulate a realistic load torque profile for an agricultural vehicle, which typically travels over an uneven ground. The time behaviors of the angular speeds ω_i of the Ravigneaux planetary gear set, as well as the desired angular speeds ω_{c_d} and ω_{s_d} of the carrier "c" and of the small sun "s", are shown in Fig. 14. The figure clearly shows that the objective of the control is achieved: the angular speeds ω_c and ω_s follow the desired speeds ω_{c_d} and ω_{s_d}, respectively. Finally, the time behaviors of the torques τ_i and of the forces F_{ij} of the Ravigneaux planetary gear set are shown in Fig. 15.

The simulation results shown in Fig. 13, Fig. 14 and Fig. 15 have been obtained using the reduced-order model (22) of the Ravigneaux planetary gear set, together with Eq. (26) in Prop. 3 for the offline calculation of the contact forces. The same simulation has also been performed using the full model (1): the corresponding simulation results are not reported in this paper because they almost coincide with the ones reported in Fig. 13, Fig. 14 and Fig. 15. The resulting simulation times obtained using a "`ode23s (stiff/Mod. Rosenbrock)`" variable-step solver are the following: 57.43 s using the full model and 29.95 s using the reduced-order model. The simulation times could change by employing a different computer and/or a different version of Matlab/Simulink, but still the result clearly shows the saving in terms of simulation time given by the use of the reduced-order model with respect to the full one.

The power-split architecture in Fig. 11 has also been simulated using a "`ode4 (Runge/Kutta)`" fixed-step solver with a step size of 10^{-4} s. The obtained simulation time using the reduced-order model of the Ravigneaux planetary gear set in the considered hybrid architecture is 7.24 s. The corresponding simulation results are not reported in this paper because they almost coincide with the ones reported in Fig. 13, Fig. 14 and Fig. 15. The simulation using the full model could not be terminated with the considered step size due to the high-frequency internal dynamics caused by the high stiffness of the planetary gear set contact points, meaning that a lower step size is needed when using the full model.

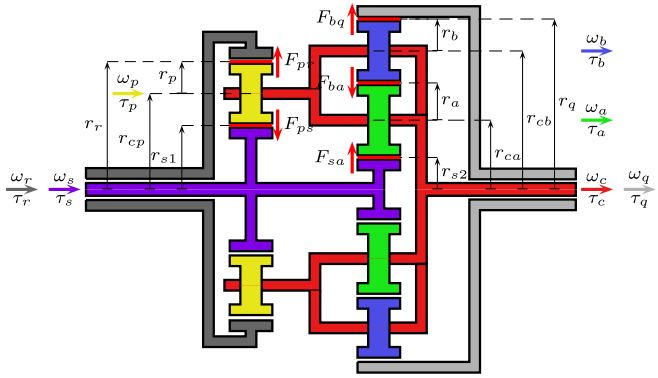

Fig. 16. Structure of the considered double-stage planetary gear set.

In conclusion, both the full and the reduced-order dynamic models of the planetary gear set are suitable for being used in the simulation of HEVs, but with different purposes. The full model represents a more detailed modeling of the planetary gear set, because it accounts for the gears elastic contact points as well. On the other hand, the reduced-order model is more suitable for real-time execution, because it allows to use fixed-step solvers with a larger step size.

IV. Modeling a Double-Stage Planetary Gear Set

Let us now consider the double-stage planetary gear set shown in Fig. 16. For this system, the sets $\mathcal{N}_J$, $\mathcal{N}_K$, $\mathcal{N}_B$ and the parameters n_J, n_K, n_B defined at the beginning of Section III are:

$$\begin{cases} \mathcal{N}_J = \{s,\, c,\, p,\, a,\, r,\, b,\, q\}, & n_J = \dim(\mathcal{N}_J) = 7, \\ \mathcal{N}_K = \{sp,\, sa,\, pr,\, ba,\, bq\}, & n_K = \dim(\mathcal{N}_K) = 5, \\ \mathcal{N}_B = \{sr,\, ca,\, cb,\, cp,\, cq\}, & n_B = \dim(\mathcal{N}_B) = 5. \end{cases} \tag{31}$$

The considered system can be modeled using the POG scheme shown in Fig. 3. Let us choose the speed vector $\boldsymbol{\omega}$, the input torque vector $\boldsymbol{\tau}$ and the force vector $\mathbf{F}$ as follows:

$$\boldsymbol{\omega} = \begin{bmatrix} \omega_s \\ \omega_c \\ \omega_p \\ \omega_a \\ \omega_r \\ \omega_b \\ \omega_q \end{bmatrix}, \quad \boldsymbol{\tau} = \begin{bmatrix} \tau_s \\ \tau_c \\ \tau_p \\ \tau_a \\ \tau_r \\ \tau_b \\ \tau_q \end{bmatrix}, \quad \mathbf{F} = \begin{bmatrix} F_{ps} \\ F_{sa} \\ F_{pr} \\ F_{ba} \\ F_{bq} \end{bmatrix}. \tag{32}$$

The order of the speed variables ω_i and of the force variables F_{ij} within vectors $\boldsymbol{\omega}$ and $\mathbf{F}$ in (32) completely defines the structures of the following matrices $\mathbf{J}$, $\mathbf{B}_\omega$, $\mathbf{K}$ and $\mathbf{B}_K$:

$$\begin{aligned} \mathbf{J} &= \operatorname{diag}(J_s,\, J_c,\, J_p,\, J_a,\, J_r,\, J_b,\, J_q), \\ \mathbf{B}_\omega &= \operatorname{diag}(b_s,\, b_c,\, b_p,\, b_a,\, b_r,\, b_b,\, b_q), \\ \mathbf{K} &= \operatorname{diag}(K_{ps},\, K_{sa},\, K_{pr},\, K_{ba},\, K_{bq}), \\ \mathbf{B}_K &= \operatorname{diag}(d_{ps},\, d_{sa},\, d_{pr},\, d_{ba},\, d_{bq}). \end{aligned}$$

The radii matrix $\mathbf{R}$ can be easily obtained using the rules given in Prop. 1:

$$\mathbf{R}=\begin{array}{c} \\ ps \\ sa \\ pr \\ ba \\ bq \end{array}\!\!\begin{array}{c} \begin{array}{ccccccc} s & c & p & a & r & b & q \end{array} \\ \begin{bmatrix} -r_{s1} & r_{cp} & -r_p & 0 & 0 & 0 & 0 \\ r_{s2} & -r_{ca} & 0 & r_a & 0 & 0 & 0 \\ 0 & r_{cp} & r_p & 0 & -r_r & 0 & 0 \\ 0 & r_{cb}-r_{ca} & 0 & -r_a & 0 & -r_b & 0 \\ 0 & r_{cb} & 0 & 0 & 0 & r_b & -r_q \end{bmatrix} \end{array}. \tag{33}$$

The parameters within the radii matrix $\mathbf{R}$ in (33) are constrained as follows:

$$\begin{aligned} r_r &= 2r_p + r_{s1}, \\ r_{cp} = \ r_p + r_{s1},\ r_{cb} &= \ 2r_a + r_b + r_{s2}, \\ r_{ca} = \ r_a + r_{s2},\ r_q &= \ 2r_a + 2r_b + r_{s2}, \end{aligned}$$

where the constraints can be easily extracted from Fig. 16. The relative friction matrix $\mathbf{B}_{\Delta\omega}$ can be obtained using the rules given in Prop. 2, and results to be the following:

$$\mathbf{B}_{\Delta\omega}=\begin{array}{c} \\ s \\ c \\ p \\ a \\ r \\ b \\ q \end{array}\!\!\begin{array}{c} \begin{array}{ccccccc} s & c & p & a & r & b & q \end{array} \\ \begin{bmatrix} b_{sr} & 0 & 0 & 0 & -b_{sr} & 0 & 0 \\ 0 & b_{ca}+b_{cb}+b_{cp}+b_{cq} & -b_{cp} & -b_{ca} & 0 & -b_{cb} & -b_{cq} \\ 0 & -b_{cp} & b_{cp} & 0 & 0 & 0 & 0 \\ 0 & -b_{ca} & 0 & b_{ca} & 0 & 0 & 0 \\ -b_{sr} & 0 & 0 & 0 & b_{sr} & 0 & 0 \\ 0 & -b_{cb} & 0 & 0 & 0 & b_{cb} & 0 \\ 0 & -b_{cq} & 0 & 0 & 0 & 0 & b_{cq} \end{bmatrix} \end{array}. \tag{34}$$

When $\mathbf{K} \to \infty$, from the state space model (1) one obtains the following constraints on the gears speeds:

$$\mathbf{R}\,\boldsymbol{\omega} = \mathbf{0} \ \Leftrightarrow \ \begin{cases} r_{cp}\,\omega_c - r_p\,\omega_p - r_{s1}\,\omega_s = 0, \\ r_a\,\omega_a - r_{ca}\,\omega_c + r_{s2}\,\omega_s = 0, \\ r_{cp}\,\omega_c + r_p\,\omega_p - r_r\,\omega_r = 0, \\ -r_a\,\omega_a - r_b\,\omega_b - \omega_c(r_{ca} - r_{cb}) = 0, \\ r_b\,\omega_b + r_{cb}\,\omega_c - r_q\,\omega_q = 0. \end{cases} \tag{35}$$

These constraints can be used to obtain the reduced-order rigid model for the considered system when $\mathbf{K} \to \infty$. Choosing $\mathbf{x}_1 = [\omega_s \ \omega_r]^{\mathrm{T}}$ and applying the following state space congruent transformation to system (1):

$$\mathbf{x} = \mathbf{T}_1\,\mathbf{x}_1 \quad \Leftrightarrow \quad \underbrace{\begin{bmatrix} \boldsymbol{\omega} \\ \mathbf{F} \end{bmatrix}}_{\mathbf{x}} = \underbrace{\begin{bmatrix} \mathbf{Q}_1 \\ \mathbf{0} \end{bmatrix}}_{\mathbf{T}_1} \underbrace{\begin{bmatrix} \omega_s \\ \omega_r \end{bmatrix}}_{\mathbf{x}_1},$$

where the matrix $\mathbf{Q}_1$ has the following structure:

$$\mathbf{Q}_1 = \begin{bmatrix} 1 & 0 \\ \frac{r_{s1}}{2r_{cp}} & \frac{r_r}{2r_{cp}} \\ -\frac{r_{s1}}{2r_p} & \frac{r_r}{2r_p} \\ \frac{r_{ca}r_{s1}-2r_{cp}r_{s2}}{2r_a r_{cp}} & \frac{r_{ca}r_r}{2r_a r_{cp}} \\ 0 & 1 \\ \frac{r_{cb}r_{s1}-2r_{ca}r_{s1}+2r_{cp}r_{s2}}{2r_b r_{cp}} & -\frac{2r_{ca}r_r-r_{cb}r_r}{2r_b r_{cp}} \\ \frac{r_{cb}r_{s1}-r_{ca}r_{s1}+r_{cp}r_{s2}}{r_{cp}r_q} & -\frac{r_{ca}r_r-r_{cb}r_r}{r_{cp}r_q} \end{bmatrix}, \tag{36}$$

one obtains a reduced-order rigid model having the same structure as the model given in (22) and (23), obtained in the previous section. The analytical expressions of the elements L_{ij} and a_{ij} within matrices $\mathbf{L}_1$ and $\mathbf{A}_1$ are not given for the sake of brevity and can be computed using (23).

TABLE III
DOUBLE-STAGE PLANETARY GEAR SET: SIMULATION PARAMETERS

$r_r = 13$ cm	$J_c = 1891000$ kg mm^2
$r_{s1} = 5.4$ cm	$J_p = 3832.1$ kg mm^2
$r_{s2} = 2.6$ cm	$J_r = 157470$ kg mm^2
$r_p = 3.8$ cm	$J_s = 6251$ kg mm^2
$r_a = 5.8$ cm	$J_a = 20798$ kg mm^2
$r_b = 5$ cm	$J_b = 11486$ kg mm^2
$r_{cp} = 9.2$ cm	$J_q = 2521300$ kg mm^2
$r_{ca} = 8.4$ cm	$r_{cb} = 19.2$ cm
$r_q = 24.2$ cm	$b_c = b_p = b_r = b_s = 0$
$b_a = b_b = b_q = b_c = 0$	$b_{cp} = 0.1$ Nm/rpm
$b_{ca} = b_{cb} = b_{cq} = b_{sr} = 0$	$K_{ps} = K_{sa} = 200$ N/mm
$K_{pr} = K_{ba} = K_{bq} = K_{ps}$	$d_{ps} = d_{sa} = 30$ N s/cm
$d_{pr} = d_{ba} = d_{bq} = d_{ps}$	$\boldsymbol{\tau} = [\,0\ 0\ 0\ 0\ 0\ 0\,]^{\mathrm{T}}$Nm
$\boldsymbol{\omega}_0 =$ see Eq. (37)	$\mathbf{F}_0 = [\,0\ 0\ 0\ 0\ 0\,]^{\mathrm{T}}$ N

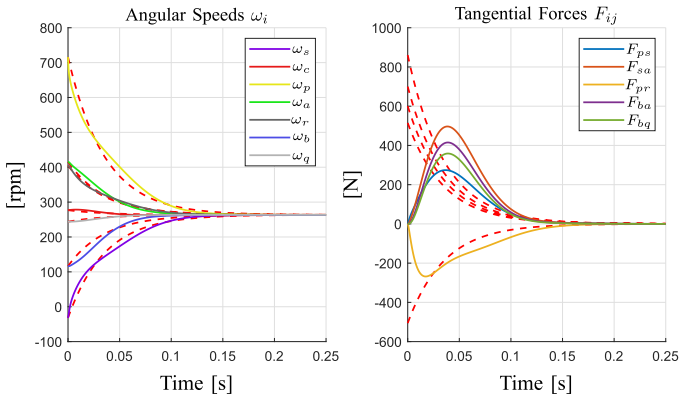

Fig. 17. Simulation of the double-stage planetary gear set.

A. Double-Stage Planetary Gear Set: Simulation Results

The double-stage planetary gear set shown in Fig. 16 has been simulated using the parameters, input signals and initial conditions shown in Table III. Even in this case, the time behavior of the full elastic model (1) has been compared with the time behavior of the reduced-order rigid model (22). Note that: the input torque vector $\boldsymbol{\tau}$ is set to zero, $\boldsymbol{\tau} = [0\ \ldots]$; the initial condition of the force vector $\mathbf{F}$ is set to zero, $\mathbf{F}_0 = [0\ \ldots]$; all the friction coefficients b_i, for $i \in \mathcal{N}_J$, are set to zero; all the relative friction coefficients b_{ij}, for $ij \in \mathcal{N}_B$, are set to zero except for $b_{cp} = 0.1$ Nm/rpm. Furthermore, the following initial condition $\boldsymbol{\omega}_0$ of the speed vector $\boldsymbol{\omega}$:

$$\boldsymbol{\omega}_0 = [-31.9 \ \ 277 \ \ 715.9 \ \ 415.4 \ \ 405.3 \ \ 116.4 \ \ 243.8]^{\mathrm{T}}\ \text{rpm}, \tag{37}$$

has been chosen to satisfy the constraint $\mathbf{R}\,\boldsymbol{\omega} = 0$ imposed by the reduced-order rigid model.

The obtained simulations results are shown in Fig. 17 and Fig. 18. The angular speeds ω_i, for $i \in \mathcal{N}_J$, are reported in the left subplot of Fig. 17, whereas the tangential forces F_{ij}, for $ij \in \mathcal{N}_K$, are reported in the right subplot. The continuous colored lines refer to the time behaviors obtained using the full elastic model (1). The dashed red lines refer to the results obtained using

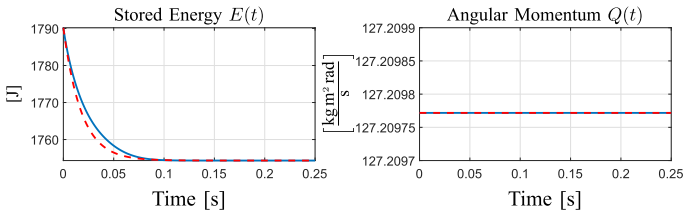

Fig. 18. Stored energy $E(t)$ and angular momentum $Q(t)$.

the reduced-order rigid model (22). Note that, for the reduced-order model, the red dashed plots of the tangential forces F_{ij} on the right subplot have been computed offline using (26). From Fig. 17, the good matching between the time behaviors obtained using the full and the reduced-order models, especially at steady-state, can be appreciated. Since all the direct and the relative friction coefficients b_j and b_{ij} have been set to zero except for the coefficient b_{cp}, all the angular speeds ω_i tend to be constant and equal to each other at steady-state. Additionally, all the forces F_{ij} tend to zero. This is exactly the case of a closed lockup clutch acting between gears "c" and "p", thus simulating the operation of the transmission in direct drive mode. The right subplot of Fig. 17 shows the stretched oscillating behavior of the tangential forces F_{ij}. This is due to the fact that the stiffness coefficients of the tangential springs K_{ij} reported in Table. III are quite low, i.e. the system exhibits a high elasticity. This choice was intentionally made to highlight the impact that the tangential springs can have on the system. The full model is therefore more suitable for being used when accurate simulations of the tangential forces are required. On the other hand, the reduced-order model is to be used when real-time execution is demanded. Fixed-step simulations are enabled by the reduced-order model, because the fast dynamics associated with the tangential springs are no longer present. However, the average time behavior of the tangential forces when using the reduced-order model can still be computed thanks to Prop. 3. Note that the initial values of the tangential forces given by the full and reduced-order models in the right subplot of Fig. 17 are initially different: this is due to the fact that the initial conditions for the tangential forces F_{ij} in the full model have been set to zero, as shown in Table III. Using the POG modeling approach [19], the energy $E(t)$ stored in the system and the angular momentum $Q(t)$ of the mechanical part of the system can be expressed as follows:

$$E(t) = \frac{1}{2}\,\mathbf{x}(t)^{\mathrm{T}}\mathbf{L}\mathbf{x}(t), \qquad Q(t) = [1\ \ldots\ 1]^{\mathrm{T}}\mathbf{J}\omega(t).$$

The time behaviors of the stored energy $E(t)$ and of the angular momentum $Q(t)$ are shown in Fig. 18. The stored energy $E(t)$ tends to a constant value, whereas the angular momentum $Q(t)$ remains constant during the simulation, since there are no external inputs acting on the system, as shown in Table III. The light blue lines in Fig. 18 refer to the full elastic model (1), whereas the red dashed lines refer to the reduced-order rigid model (22).

V. Conclusion

In this paper, a systematic methodology for modeling planetary gear sets has been presented. The proposed approach relies upon a general model, which can be used to model any planetary gear set and is directly implementable in the Matlab/Simulink environment. All the system matrices and vectors are either automatically defined or directly computable using the two presented algorithms. The potentiality of inserting some relative friction between any two of the system gears allows to insert lockup clutches in the planetary gear set, thus allowing to simulate different operating modes of the transmission system. The proposed approach allows to obtain two dynamic models of the system: a full elastic model accounting for the gears elastic interaction and a reduced-order rigid model. The first one is suitable for accurately simulating the system, whereas the second one is suitable for fixed-step simulations which are needed for real-time execution. In the reduced-order model, the time behavior of the tangential forces can still be recovered, even if they are no longer present in the system. Furthermore, the kinematic speed and torque equations automatically turn out when the reduced-order model is computed. The proposed modeling approach has been applied to two case studies implemented in the Matlab/Simulink environment: a Ravigneaux planetary gear set and a double-stage planetary gear set. The full and reduced-order models of the Ravigneaux planetary gear set have also been tested in simulation when mounted in a power-split architecture of a HEV, in order to simulate a real case scenario. The simulation results show the good superposition between the results given by the full and the reduced-order models, and point out the gain which has been achieved in terms of simulation time thanks to the reduced-order model.

Appendix
Proof of Property 3

The first equation of (1) can be rewritten as follows:

$$\mathbf{R}^{\mathrm{T}}\mathbf{F} = \boldsymbol{\tau} - \mathbf{J}\,\dot{\boldsymbol{\omega}} - (\mathbf{B}_J + \mathbf{R}^{\mathrm{T}}\mathbf{B}_k\mathbf{R})\,\boldsymbol{\omega}. \tag{38}$$

When $\mathbf{K} \to \infty$, from (19) and (20) it follows: $\boldsymbol{\omega} = \mathbf{Q}_1\mathbf{x}_1$. Replacing $\boldsymbol{\omega}$ in (38), one obtains:

$$\mathbf{R}^{\mathrm{T}}\mathbf{F} = \underbrace{\boldsymbol{\tau} - \mathbf{J}\,\mathbf{Q}_1\dot{\mathbf{x}}_1 - \mathbf{B}_J\mathbf{Q}_1\mathbf{x}_1}_{\bar{\boldsymbol{\tau}}} - \mathbf{R}^{\mathrm{T}}\mathbf{B}_k\,\underbrace{\mathbf{R}\mathbf{Q}_1}_{\mathbf{0}}\,\mathbf{x}_1. \tag{39}$$

The last term of (39) is equal to zero because $\mathbf{R}\mathbf{Q}_1 = 0$, see (24). By substituting the time derivative $\dot{\mathbf{x}}_1 = \mathbf{L}_1^{-1}\mathbf{A}_1\,\mathbf{x}_1 + \mathbf{L}_1^{-1}\mathbf{B}_1\,\boldsymbol{\tau}$ obtained from the reduced system (22) in (39), one obtains:

$$\mathbf{R}^{\mathrm{T}}\mathbf{F} = (\mathbf{I} - \mathbf{J}\mathbf{Q}_1\mathbf{L}_1^{-1}\mathbf{Q}_1^{\mathrm{T}})\boldsymbol{\tau} - (\mathbf{B}_J\mathbf{Q}_1 + \mathbf{J}\mathbf{Q}_1\mathbf{L}_1^{-1}\mathbf{A}_1)\mathbf{x}_1. \tag{40}$$

By substituting the expressions of matrices $\mathbf{L}_1$ and $\mathbf{A}_1$ given in (23) within (40), one obtains the following relation:

$$\begin{aligned}\mathbf{R}^{\mathrm{T}}\mathbf{F} = {} & (\mathbf{I} - \mathbf{J}\mathbf{Q}_1(\mathbf{Q}_1^{\mathrm{T}}\mathbf{J}\mathbf{Q}_1)^{-1}\mathbf{Q}_1^{\mathrm{T}})\boldsymbol{\tau} + \\ & - (\mathbf{B}_J\mathbf{Q}_1 - \mathbf{J}\mathbf{Q}_1(\mathbf{Q}_1^{\mathrm{T}}\mathbf{J}\mathbf{Q}_1)^{-1}\mathbf{Q}_1^{\mathrm{T}}\mathbf{B}_J\mathbf{Q}_1)\mathbf{x}_1.\end{aligned} \tag{41}$$

The latter relation can be easily rewritten as follows:

$$\mathbf{R}^{\mathrm{T}}\mathbf{F} = \underbrace{(\mathbf{I} - \mathbf{J}\mathbf{Q}_1(\mathbf{Q}_1^{\mathrm{T}}\mathbf{J}\mathbf{Q}_1)^{-1}\mathbf{Q}_1^{\mathrm{T}})}_{\mathbf{M}_p}(\boldsymbol{\tau} - \mathbf{B}_J\mathbf{Q}_1\mathbf{x}_1). \tag{42}$$

Let functions $\mathrm{Im}(\mathbf{A})$ and $\ker(\mathbf{A})$ denote the image and the kernel of matrix $\mathbf{A}$, respectively. From linear matrix algebra, it is well

known that matrix $\mathbf{M}_p$ in (42) is a projection matrix on $\ker(\mathbf{Q}_1^{\mathrm{T}})$ along $\mathrm{Im}(\mathbf{JQ}_1)$. From (19) and (20), it follows that: $\mathbf{R}\boldsymbol{\omega} = \mathbf{0} \leftrightarrow \mathbf{RQ}_1\mathbf{x}_1 = \mathbf{0} \leftrightarrow \mathbf{RQ}_1 = \mathbf{0} \leftrightarrow \mathbf{Q}_1^{\mathrm{T}}\mathbf{R}^{\mathrm{T}} = \mathbf{0}$, which implies that $\ker(\mathbf{Q}_1^{\mathrm{T}}) = \mathrm{Im}(\mathbf{R}^{\mathrm{T}})$. Furthermore, it is true that $\mathrm{Im}(\mathbf{JQ}_1) = \ker(\mathbf{S}^{\mathrm{T}})$, where $\mathbf{S}$ is a matrix such that $\mathrm{Im}(\mathbf{S}) = \ker[(\mathbf{JQ}_1)^{\mathrm{T}}] = \ker(\mathbf{Q}_1^{\mathrm{T}}\mathbf{J})$. From $\mathbf{Q}_1^{\mathrm{T}}\mathbf{R}^{\mathrm{T}} = \mathbf{0}$, it follows that $\mathbf{Q}_1^{\mathrm{T}}\mathbf{J}\mathbf{J}^{-1}\mathbf{R}^{\mathrm{T}} = \mathbf{0}$, which implies that $\ker(\mathbf{Q}_1^{\mathrm{T}}\mathbf{J}) = \mathrm{Im}(\mathbf{J}^{-1}\mathbf{R}^{\mathrm{T}}) = \mathrm{Im}(\mathbf{S})$. From the previous considerations, it follows that $\mathbf{M}_p$ can be rewritten as reported in the following:

$$\mathbf{M}_p = \mathbf{R}^{\mathrm{T}}(\mathbf{S}^{\mathrm{T}}\mathbf{R}^{\mathrm{T}})^{-1}\mathbf{S}^{\mathrm{T}} = \mathbf{R}^{\mathrm{T}}(\mathbf{R}\mathbf{J}^{-1}\mathbf{R}^{\mathrm{T}})^{-1}\mathbf{R}\mathbf{J}^{-1}. \tag{43}$$

Substituting (43) in (42), one obtains:

$$\mathbf{R}^{\mathrm{T}}\mathbf{F} = \mathbf{R}^{\mathrm{T}}(\mathbf{R}\mathbf{J}^{-1}\mathbf{R}^{\mathrm{T}})^{-1}\mathbf{R}\mathbf{J}^{-1}(\boldsymbol{\tau} - \mathbf{B}_J\mathbf{Q}_1\mathbf{x}_1), \tag{44}$$

which directly implies the relation given in (26), since $\mathbf{R}^{\mathrm{T}}$ is a full rank matrix. □

REFERENCES

[1] J. M. Miller, "Hybrid electric vehicle propulsion system architectures of the e-CVT type," *IEEE Trans. Power Electron.*, vol. 21, no. 3, pp. 756–767, May. 2006.

[2] A. Zia, "A comprehensive overview on the architecture of hybrid electric vehicles (HEV)," *Proc. 19th Int. Multi-Topic Conf.*, Islamabad, Pakistan, Dec., 2016, pp. 5–6.

[3] M. Ducusin, S. Gargies, and C. Mi, "Modeling of a series hybrid electric high-mobility multipurpose wheeled vehicle," *IEEE Trans. Veh. Technol.*, vol. 56, no. 2, pp. 557–565, Mar. 2007.

[4] N. Denis, M. R. Dubois, J. Pedro F. Trovão, and A. Desrochers, "Power split strategy optimization of a plug-in parallel hybrid electric vehicle," *IEEE Trans. Veh. Technol.*, vol. 67, no. 1, pp. 315–326, Jan. 2018.

[5] J. Liu and H. Peng, "Modeling and control of a power-split hybrid vehicle," *IEEE Trans. Control Syst. Technol.*, vol. 16, no. 6, pp. 1242–1251, Nov. 2008.

[6] D. Tebaldi and R. Zanasi, "Modeling and control of a power-split hybrid propulsion system," *Proc. IEEE 45th Annu. Conf. Ind. Electron. Soc.*, Lisbon, Portugal, Oct. 14–17, 2019.

[7] Y. D. Setiawan, M. Roozegar, T. Zou, and J. Angeles, "A mathematical model of multispeed transmissions in electric vehicles in the presence of gear shifting," *IEEE Trans. Veh. Technol.*, vol. 67, no. 1, pp. 397–408, Jan. 2018.

[8] W. Guo, C. Chen, and X. Li, "A modified dynamic model for a two-stage planetary gearbox with tooth cracks and its vibration analyses," *Proc. Int. Conf. Sens., Diagnostics, Prognostics, Control*, Shanghai, China, Aug. 16–18, 2017.

[9] S. A. Syed, W. Lhomme, A. Bouscayrol, O. Pape, and G. LeTrouher, "Modeling of power split device for heavy-duty vehicles," *Proc. IEEE Veh. Power Propulsion Conf.*, Lille, France, Sep. 1–3, 2010.

[10] S. A. Syed, W. Lhomme, and A. Bouscayrol, "Modeling of power split device with clutch for heavy-duty millitary vehicles," *Proc. IEEE Veh. Power Propulsion Conf.*, Chicago, IL, USA, Sep. 6–9, 2011.

[11] W. Lhomme, A. Bouscayrol, S. A. Syed, S. Roy, F. Gailly, and O. Pape, "Energy savings of a hybrid truck using a ravigneaux gear train," *IEEE Trans. Veh. Technol.*, vol. 66, no. 10, pp. 8682–8692, Oct. 2017.

[12] F. Freudenstein and A. T. Yang, "Kinematics and statics of a coupled epicyclic spur-gear train," *Mech. Mach. Theory*, vol. 7, no. 2, pp. 263–275, 1972.

[13] H. L. Benford and M. B. Leising, "The level analogy: A new tool in transmission an alysis," *SAE Trans.*, vol. 90, no. 1, pp. 429–437, 1981.

[14] X. Zhang, C.-T. Li, D. Kum, and H. Peng, "Prius^{+} and Volt^{-}: Configuration analysis of power-split hybrid vehicles with a single planetary gear," *IEEE Trans. Veh. Technol.*, vol. 61, no. 8, pp. 3544–3552, Oct. 2012.

[15] X. Zhang, H. Peng, and J. Sun, "A near-optimal power management strategy for rapid component sizing of multimode power split hybrid vehicles," *IEEE Trans. Control Syst. Technol.*, vol. 23, no. 2, pp. 609–618, Mar. 2015.

[16] L. Yang, M. Hu, D. Qin, A. Zhou, C. Fu, and M. Yu, "Analysis and optimization of a novel power-split hybrid powertrain," *IEEE Trans. Veh. Technol.*, vol. 68, no. 11, pp. 10504–10517, Nov. 2019.

[17] J. Zhang, T. Shen, and J. Kako, "Short-term optimal energy management of power-split hybrid electric vehicles under velocity tracking control," *IEEE Trans. Veh. Technol.*, vol. 69, no. 1, pp. 182–193, Jan. 2020.

[18] R. Zanasi, G. H. Geitner, A. Bouscayrol, and W. Lhomme, "Different energetic techniques for modelling traction drives," *Proc. 9th Int. Conf. Model. Simul. Electric Mach., Converters Syst.*, Québec, Canada, Jun. 8-11, 2008.

[19] R. Zanasi, "The power-oriented graphs technique: System modeling and basic properties," *Proc. IEEE Veh. Power Propulsion Conf.*, Lille, France, Sep. 2010, pp. 1–3.

[20] M. Fei, R. Zanasi, and F. Grossi, "Modeling of multi-phase permanent magnet Synchronous motors under open-phase fault condition," *Proc. IEEE Int. Conf. Control Autom.*, Santiago, Chile, Dec. 2011, pp. 19–21.

[21] R. Zanasi and F. Grossi, "The POG technique for modeling planetary gears and hybrid automotive systems," *Proc. IEEE Veh. Power Propulsion Conf.*, Dearborn, MI, USA, Sep. 2009, pp. 7–10.

[22] R. Zanasi and D. Tebaldi, "Planetary gear modeling using the power-oriented graphs technique," *Proc. IEEE Eur. Control Conf.*, Naples, Italy, Jun. 2019, pp. 25–28.

[23] Y. G. Liao and M.-Y. Chen, "Analysis of multi-speed transmission and electrically continuous variable transmission using lever analogy method for speed ratio determination," *Adv. Mech. Eng.*, vol. 9, no. 8, pp. 1–12, 2017.

Roberto Zanasi (Member, IEEE) was born in Bomporto (MO), Italy, in 1959. He Graduated (with Hons.) in electrical engineering from the University of Bologna in 1986. He received the Ph.D. degree in system engineering in 1992. From 1994 to 1998, he was Researcher in automatic control with the Department of Electronics, Computer and System Science, University of Bologna. Since 1998, he has been working as an Associate Professor of Automatic Control with the "Dipartimento di Ingegneria dell'Informazione," University of Modena and Reggio Emilia. From 2004, he is Full Professor in automatic control with the "Enzo Ferrari" Department of Engineering, University of Modena and Reggio Emilia. He held the position of Visiting Scientist with the IRIMS of Moscow in 1991, at the MIT of Boston in 1992 and at the Université Catholique de Louvain in 1995. He is authored or coauthored of many technical and scientific publications, and of five books on automatic control, simulation and digital control systems. His research interests include: mathematical modeling, power-oriented graphs, simulation, automotive, control of multi-phase electrical motors, variable-structure systems, sliding mode control with integral action, robotics, linear and nonlinear control, etc.

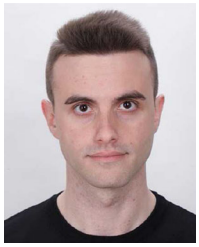

Davide Tebaldi was born in Pavullo nel Frignano (MO), Italy, in 1992. He received the B.S. and M.S. degrees *(cum laude)* in electronic engineering from the University of Modena and Reggio Emilia, Italy, in 2015 and 2018, respectively. He is currently working toward the Ph.D. degree in information and communications technologies with the University of Modena and Reggio Emilia. His research interests include energetic modeling, control and simulation of mechatronic systems, with main application in automotive, electrical machines and power electronics fields.